Chapter 4

Fabrication and Characterization of p-Silicon Nanowire/n-TiO_2 Heterojunction Diodes Grown by Sol-Gel and E-Beam Evaporation Methods for Optoelectronic Applications

4.1 Introduction

Silicon Nanowires (SiNWs) have drawn significant attention for applications in nanoelectronic devices including solar cells, gas sensors, memory devices, photodetectors and thermoelectric devices [Abramson *et al.* (2004), Chakrabartty *et al.* (2014), Rasool *et al.* (2015), Akgul *et al.* (2016)]. The literature survey presented in Chapter-1 shows that 1D nanostructured heterojunctions are preferred over bulk heterojunctions devices for various sensing applications due to their larger surface-to-volume ratio, better carrier transport properties [Yu *et al.* (2009-a)] and higher charge separation ability of photo-generated carriers in optoelectronic devices [Yu *et al.* (2009-b), Shougaijam *et al.* (2016)]. It is also observed from the literature survey that the chemical etching is perhaps the simplest low-cost and low-temperature synthesis technique for the fabrication of SiNWs [Peng *et al.* (2006-b), Hazra and Jit (2013)]. In view of the above, after considering the p-Si(bulk)/n-TiO_2 heterojunction diodes in Chapter-2, the present Chapter has been devoted for studying the electrical and optical properties p-Si(bulk)/p-SiNWs/n-TiO_2 thin film (TF) heterojunction photodiodes prepared by using EBE and SG deposition methods for the coating of TiO_2 films on SiNWs grown on the p-Si <100> substrate by Electroless Metal Deposition and Etching (EMDE) method. The proposed core-shell p-SiNWs/n-TiO_2 TF heterojunction structure

has been explored for UV detection applications. The outline of present chapter is given as follows:

Section 4.2 provides experimental details including substrate preparation, synthesis and growth mechanism of p-SiNW arrays, and fabrication of p-SiNW/n-TiO_2 heterojunction diodes. Section 4.3 includes surface morphology, crystallinity, optical and electrical properties of the proposed heterojunction diodes under study. Finally, Section 4.4 presents the summary and conclusion of this chapter.

4.2 Experimental Details

In the present section we will discuss the experimental details and procedure for the fabrication and characterization of p-Silicon Nanowire/n-TiO_2 heterojunction diodes considered in this chapter. The device fabrication includes substrate cleaning, synthesis of p-Silicon Nanowire arrays, TiO_2 film deposition, annealing, deposition of anode and cathode sequentially for ohmic contact formation, followed by post annealing. Figure 4.1 illustrates the layout of the fabrication steps in form of a flowchart. In the following sections first we will discuss the fabrication method then the results of characterizations.

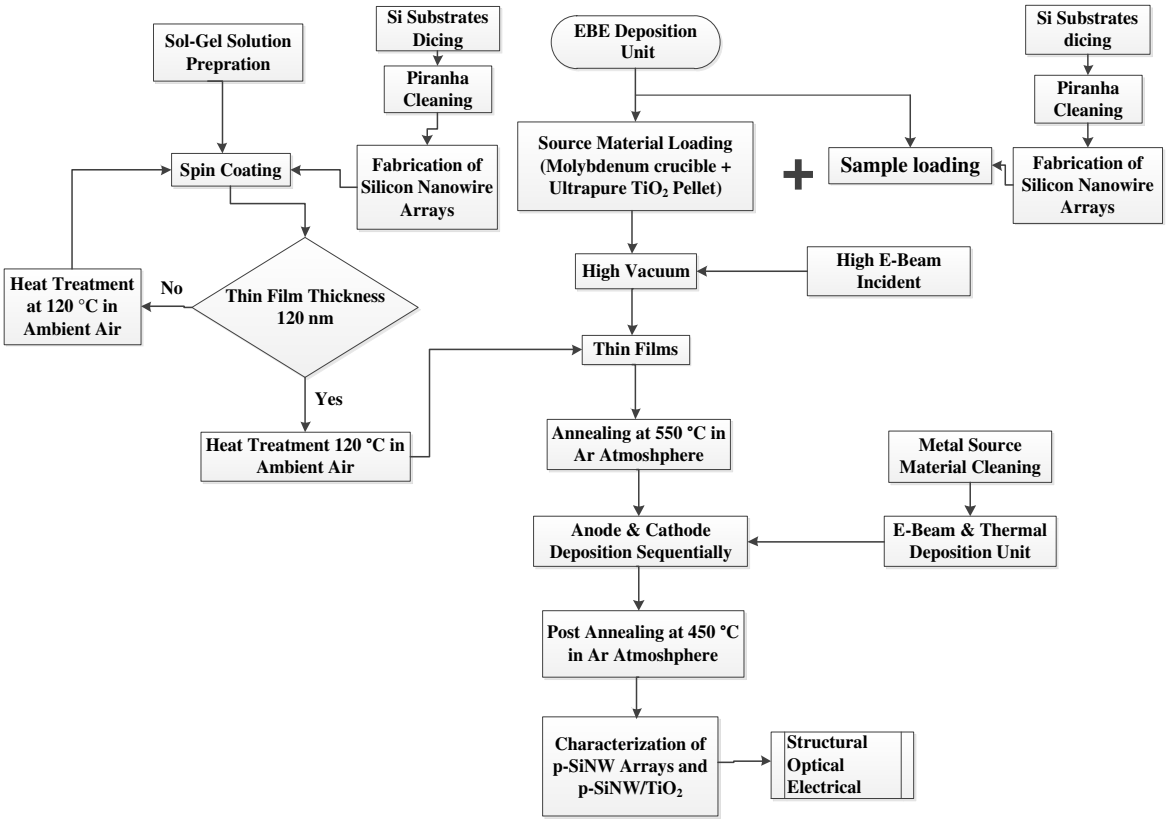

Figure 4.1: Layout of the fabrication steps for p-SiNWs/n-TiO_2 Core-Shell heterojunction diodes.

4.2.1 Substrates Cleaning

Same methodology as discussed in Chapter-2 has been adopted for the substrate preparation and cleaning of devices fabricated in this chapter. Thus experimental details of the substrate preparation and cleaning procedure are mentioned in Section 2.2.1.

4.2.2 Synthesis of p-SiNW arrays

Initailly the boron doped p-Si <100> substrates (thickness ~345 to 445 µm with resistivity ~2–7Ω.cm) were first cleaned ultrasonically in a sequence of trichloroethylene (TCE) and isopropyl alcohol for 10 min. Piranha cleaning was performed in a boiling solution of H_2SO_4: H_2O_2 (40:60) at 80 °C for 20 min. After each

step, the Si substrates were thoroughly quenched in deionized (DI) water (resistivity 18 MΩ.cm) obtained from Millipore (Model Milli-Q). All the chemicals used were purchased from MERK-Chemical Limited, Mumbai, India. Cleaned non polished surface of the p-Si wafers were coated with a thin layer of photoresist by using spin coater so that p-SiNWs could be grown only on the polished surface. The p-SiNW arrays were synthesized on the cleaned and polished surface of the p-Si substrates using the two-step process of the EMDE method [Peng *et al.* (2006-a), Hazra and Jit (2013)]. In the first step, a very thin layer of polycrystalline silver (Ag) nanoparticles were grown on the cleaned p-Si wafers by immersing them in a Teflon vessel containing a solution of analytical grade (99.9 % pure) 0.02 M silver nitrate ($AgNO_3$) and 4.6 M hydrofluoric acid (HF) for 60 seconds. First step is bascially metal (silver) catalyzed electrochemical method [Peng *et al.* (2006-a), Sivako *et al.* (2011)]. In the second step, etching process (for the Si substrates covered with silver (Ag) nanoparticles) was carried out under dark condition for 1 hr. in a Teflon vessel containing a fresh solution of 0.02 M $AgNO_3$ and 4.6 M HF at constant temperature (~50 °C) in an oven. Then after one hour of duration the top surface of Ag nanoparticles coated p-Si wafers were found to be covered with a thick and soft Ag layer (i.e silver dendrites) which was then cleaned by immersing the samples in a 30 % Nitric acid (HNO_3) solution for 20 minutes [Hazra and Jit (2013), Hazra and Jit (2014-a)]. Subsequently the samples were rinsed in DI water and then dried at 110 °C in an oven for 20 min. In further step for Ag removal, we dip the samples in a mixture solution (0.1 M) of Sodium thiosulfate ($Na_2S_2O_3$) and Isopropyl alcohol (C_3H_8O) for 20 min. duration. Here isopropyl alcohol works as a surfactant and importantly in this soultion Ag forms a soluble complex $\left(S_2O_3^{2-}\right)$ due to the presence of thiosulfate [Wittemann *et al.* (2010), Jia *et al.* (2012)]. Again samples were rinsed several times in DI water and dried. Now to clean the

photoresist coated on back surface, we dip samples in a mixed solution of TCE:Proponal:Acetic acid (in the ratio of 6:2:1 by volume). Finally, the samples were rinsed several times in DI water and dried at 110 °C in an oven for 20 min. in an inert gas environment. To avoid the formation of native oxide on p-SiNWs layer, the samples were then immediately processed for TiO_2 film deposition as described below. For simplicity and ease of understanding we have illustrated the growth of Silicon Nanowires in form of flowchart as shown in Figure 4.2.

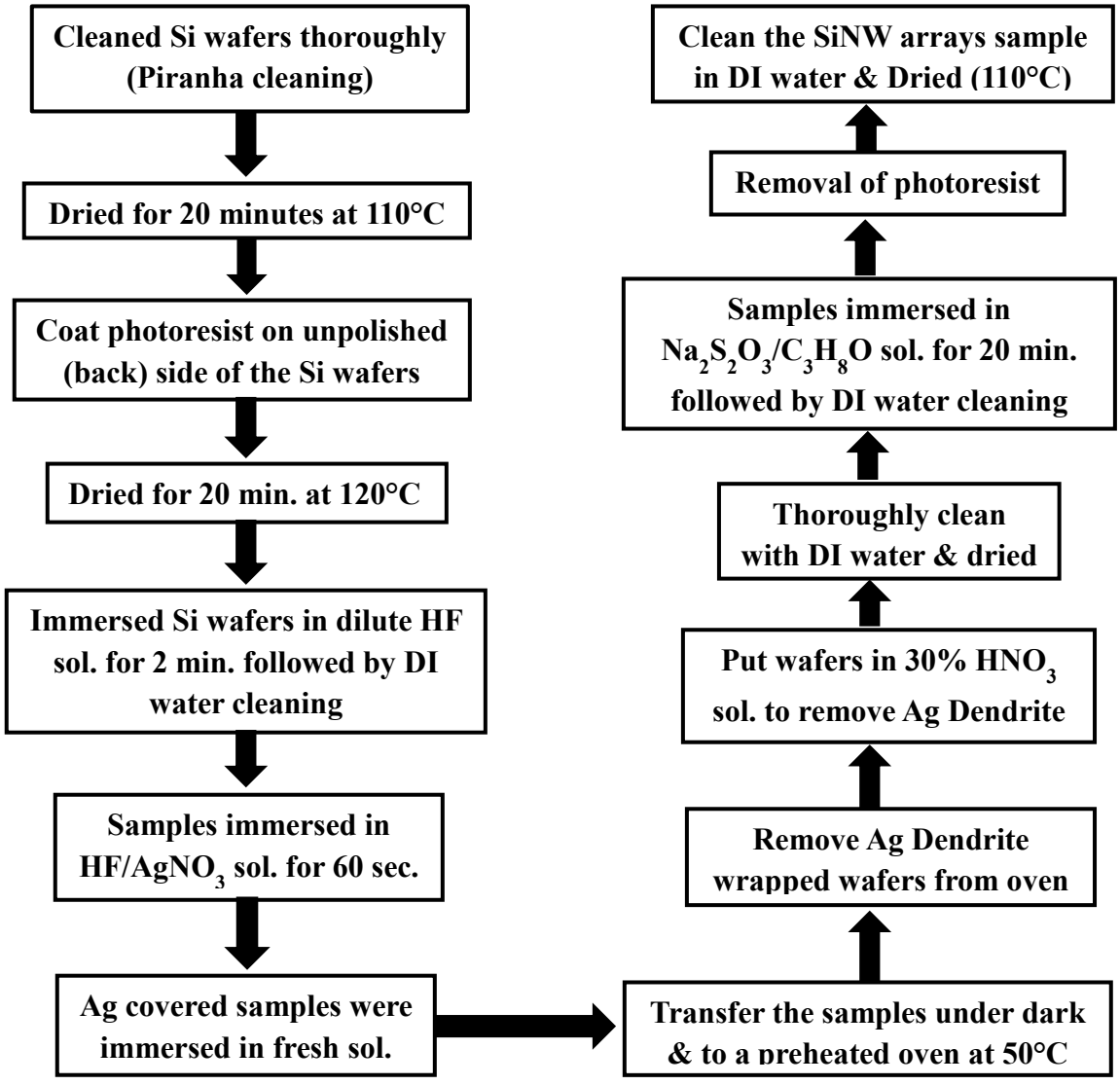

Figure 4.2: Flowchart for the Growth of Silicon Nanowires.

4.2.3 Growth Mechanism of Silicon Nanowires (SiNWs)

In the fabrication method described above, SiNWs are formed by the silver assisted electroless (chemical) etching of Si wafer with the aqueous solution of 0.02 M $AgNO_3$ and 4.6 M HF at 50 °C for one hour. In principle, the formation mechanism of SiNW arrays is based on micro-electrochemical redox reaction [Peng *et al.* (2003)] as illustrated in Figure 4.3. Metal (i.e. Ag) assisted electroless etching constitutes of two processes: (a) metal nucleation (i.e. deposition of metal nanoparticles) on Si wafer by electroless deposition for a short period of time [Peng *et al.* (2002)] and, (b) electroless etching of silicon catalyzed by the metal (i.e. Ag) particles. The first step is the metal catalyzed electrochemical process, where Ag nanoparticles are deposited on the top surface of Si wafer immersed into the active aqueous $AgNO_3$/HF mixture solution to the form metallic silver nuclei (Ag^0) as shown in Figure 4.3 (c). In the second step, the Ag ions capture electrons from Si (as described by Eq. (4.1)) thereby Si atoms surrounding to Ag nuclei are oxidized to form SiO_2 (as Eq. (4.2)) which gets dissolved by HF by forming H_2SiF_6 (as described by Eq. (4.3)). The lower energy level of Ag^0/Ag^+ than the Si valence band (VB) edge thermodynamically favours the electron transfer from Si to Ag ions (Ag^+) considered in Eq. (4.1) [Sivako *et al.* (2011)]. In other words Ag nuclei have higher electronic activity than the Si atoms [Huang *et al.* (2011), Liu *et al.* (2012-a)] so that the Ag nanoparticles and their adjacent Si atoms can act as cathodes and anodes, respectively, in the concerned electrochemical redox-reaction. The two synchronous half-cell reactions (i.e. anode and cathode reactions) can be formulated as mentioned below:

a. Cathode reaction:

$$Ag^+(aq) + e^-_{VB,Si} \rightarrow Ag^0(solid) \tag{4.1}$$

b. Anode reaction:

$$Si\,(solid) + 2H_2O \rightarrow SiO_2\,(solid) + 4H^+ + 4e^-_{VB,Si} \quad (4.2)$$

$$SiO_2\,(solid) + 6HF \rightarrow H_2SiF_6 + 2H_2O \quad (4.3)$$

After the Ag nuclei formation, Ag deposition and Si etching occur simultaneously. The overall oxidation and reduction reactions can be described as follows:

c. Overall chemical reaction:

$$4Ag^+\,(aq) + Si^0\,(solid) + 6F^-\,(aq) \rightarrow 4Aq\,(solid) + SiF_6^{2-}\,(aq) \quad (4.4)$$

After the dissolution of SiO_2 as SiF_6^{2-} (see Eq. (4.4)), pits are shaped straightaway underneath the Ag^0 nucleus so that the Ag nanoparticles go down into the pits (see Figure 4.3). The depth of the pits due to continuous falling of Ag nanoparticles (see Figure 4.3) depends on the allowed etching period of the Si substrates. Note that the lateral etching does not readily occur because the diffusion pathway for electrons to reach Ag nanoparticle is longer from the side walls than through the pore directly beneath the Ag nanoparticle [Sivako *et al.* (2011)]. In addition to time, large bulk thickness of p-Si substrates (~400 μm) and large number of Ag nanoparticles in aqueous $AgNO_3$/HF solution cause continuous occurrence of the above mentioned reactions to finally yield vertically aligned SiNW arrays. Thus, the vertically aligned and crystalline p-SiNW arrays are formed all over the p-Si substrates. However, we may also observe a thick but soft silver dendrites layer on the top of SiNWs which is removed by immersing the samples in a 30 % Nitric acid (HNO_3) solution for 20 minutes [Hazra and Jit (2013), Hazra and Jit (2014-a)]. The samples are then dipped in a mixture solution (0.1 M) of Sodium thiosulfate ($Na_2S_2O_3$) and Isopropyl alcohol for 20 min. duration for the removal of Ag nanoparticles lying inside the pits. Here isopropyl alcohol works as a surfactant which allows Ag to form a soluble complex $\left(S_2O_3^{2-}\right)$ due

to the presence of thiosulfate [Wittemann *et al.* (2010), Jia *et al.* (2012)] as described by the following chemical reaction:

$$Ag^{+}\,(\mathrm{aq}) + 2S_2O_3^{2-}\,(\mathrm{aq}) \rightarrow Ag(S_2O_3)_2^{3-}\,(\mathrm{aq}) \qquad (4.5)$$

Finally, the samples are rinsed several times in DI water and then are dried up at 110 °C in an oven for 20 min. in an inert gas environment before processing for the device fabrication and SiNWs characterizations.

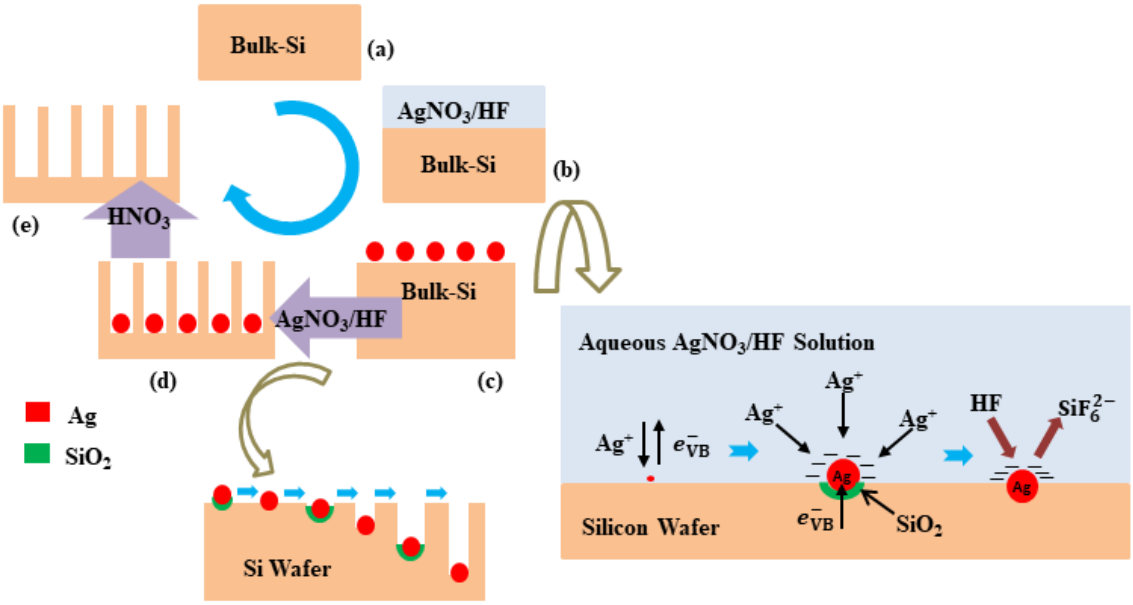

Figure 4.3: Schematic illustration of possible mechanism for the growth of SiNWs arrays.

4.2.4 Fabrication of p-SiNW/n-TiO_2 Heterojunction Diodes

We have considered two deposition techniques for the fabrication of p-SiNW/n-TiO_2 Core-Shell Heterojunction Diodes. The details of experimental procedure for each technique are discussed in the following subsections.

The thickness of n-TiO_2 film is chosen to be ~120 nm to ensure the fully depletion condition of the film so that photo-generated electron-hole pairs due to incident UV

radiation are easily separated by the electric field in the depletion region of p-SiNWs/n-TiO_2 heterojunction diode. Since most of the semiconductors have very high (~10^5 cm^{-1}) absorption coefficient in the UV region with an effective absorption length of ~100 nm or less [Sze (1981)] in TiO_2 film, the film thickness of ~120 nm is believed to be sufficient for effective absorption of the UV light for its detection. Note that a larger thickness of the TiO_2 film on p-SiNWs may enhance the bulk properties of the TiO_2 material which in turn, may reduce the effective surface-to-volume ratio of the TiO_2 TF and hence the responsivity of the UV detector under study.

4.2.4.1 TiO_2 Film Deposition by EBE Method

Straightaway after the synthesis and cleaning of p-SiNW arrays (as mentioned in Section 4.2.2) the n-TiO_2 TF (~120 nm) was deposited on the as-grown p-SiNWs in the EBE unit (Model No: FL400, SMART COAT 3.0 from HINDVAC, Bangalore, India) by using TiO_2 pellet as source material. The ultrapure TiO_2 powder (99.99%) was pressed in a dice to form the pellets using Polyvinyl Alcohol (PVA) as a binder. To solidify the pellets and to decompose the PVA, pellets were heated in ambient air atmosphere at 1200 °C for 3 hours before using as the source material. The TiO_2 pellets were placed in a molybdenum crucible and vaporized in the EBE unit at high vacuum (~10^{-5} to ~10^{-6} mbar), for TiO_2 TF (of thickness ~120 nm) deposition on the substrate at a rate of ~1.00 Å/s. The depostion rate as well as the thickness of the film was monitored by the in-built digital thickness monitor (from INFICON with model number SQM-160).

4.2.4.2 TiO_2 Film Deposition by SG Method

The formation of p-SiNWs/n-TiO_2 Core Shell heterojunction diodes includes two steps:

(a) Synthesis of Sol-gel Solution: All the necessary details for SG synthesis with its relevant flow chart are already discussed in Section 2.2.3.1 (Chapter-2).

(b) TiO_2 Film Growth by Spin Coating Method: With no delay after the synthesis of p-SiNW arrays and SG solution, we used spin coating to obtain the thin TiO_2 film of thickness ~120 nm over the as grown p-SiNW arrays. The transparent TiO_2 solution was slowly poured in the form of droplets over as-synthesized cleaned p-SiNW arrays. Thereafter the substrates were rotated by the spin coater with gradual increase in spinning speed to final speed of 3000 r/min (rpm) for 30 sec. duration. Then, the spin coated p-SiNW arrays samples were kept in a pre-heated temperature controlled oven at ~120 °C for 20 min. duration. After optimization the same steps were sequentially repeated three times with the same speed and duration to achieve the desired film thickness of ~120 nm.

4.2.5 Annealing of TiO_2 Thin Films

After spin coating and the EBE deposition all the TiO_2 deposited p-SiNWs were further processed for rapid thermal annealing (RTA) at a predetermined optimum condition at 550 °C for 20 min. in the Argon atmosphere. Cyliderical quartz furnace under the Ar inert gas with a flow rate of 30 sccm was used to improve the crystalline quality of the anatase phase n-TiO_2 film on p-SiNWs [Hazra *et al.* (2014-c)]. Later all the samples were cooled down to room temperature for further processing as discussed in the following sub-section.

4.2.6 Formation of Ohmic Contacts

For fabricating ohmic contacts to p-SiNWs/n-TiO_2 heterojunction under study, suitable metal contacts (Ti/Al) were deposited on both sides of the annealed samples. EBE deposition and shadow mask technique were used for the deposition of Ti (~70 nm) and Al (~50 nm) metal dots of ~1 mm diameter, sequentially over the top surface of n-TiO_2 layer. Electrodes on the back side (i.e. opposite to TiO_2 side) of p-SiNW arrays were grown by depositing high purity (~99.99 %) Ti (~50 nm) and Al (~40 nm) contacts. Other experimental parameters were same as discussed in Section 2.2.5 (Chapter-2).

4.2.7 Post Fabrication Annealing

Finally, the above fabricated devices with ohmic contacts were processed for post fabrication annealing treatment at 450 °C for 7 min. in Ar gas atmosphere with a flow rate of argon ~30 sccm. The importance of each individual fabrication step is already discussed in Chapter-1 and Chapter-2. Finally, Figure 4.4 illustrates the schematic diagram of the fabrication procedure followed.

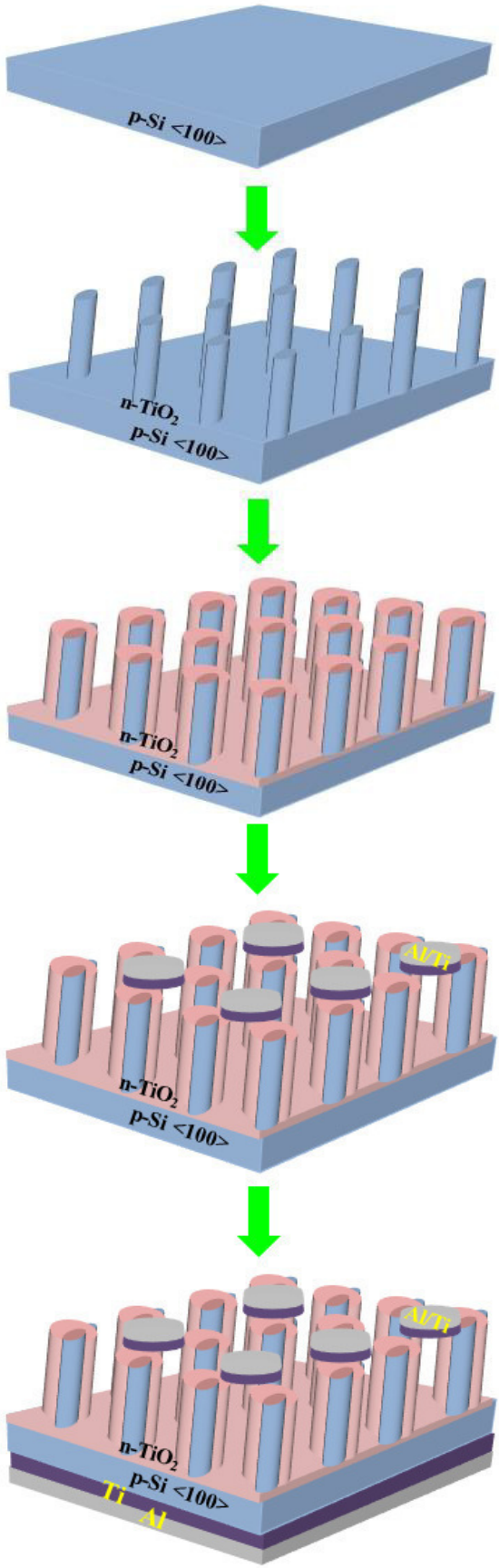

1. Cleaning of p-Si substrates by standard cleaning procedure.
2. Synthesis of p-Silicon Nanowires arrays using EMDE Technique.
3. Deposition of TiO_2 TFs (~120 nm) on p-SiNWs using two different methods:
   - ✓ *Sol-gel*
   - ✓ *E-Beam Evapouration*
4. The annealing treatment of the TiO_2 TFs is carried out in the Ar gas atmosphere at ~550 °C for 20 minutes.
5. On the top surface of TiO_2 TFs, Ti/Al contacts are deposited by EBE method using shadow mask technique.
6. On the non-polished surface of p-Si the Ti/Al contacts are deposited using EBE method.
7. After electrical contacts deposition, the post fabrication annealing is carried out in Ar gas atmosphere at ~450 °C for 7 minutes.

Figure 4.4: Flow chart for the Al/Ti/p-SiNWs/n-TiO_2/Ti/Al heterojunction diode fabrication.

4.3 Results and Discussion

4.3.1 Characterization of SiNWs

4.3.1.1 Surface Morphology and Crystallographic Structure

(a) Surface morphology study by HRSEM images

The High Resolution Scanning Electron Microscopy (HRSEM) images (Carl Zeiss Microscopy Ltd., UK) of the samples containing only p-SiNW arrays have been shown in Figure 4.5 (a) and (b). The images of Figure 4.5 (a) and (b) are for the samples after EMDE synthesis and cleaning as discussed in Section 4.2.2. Figure 4.5 (a) and (b) illustrates the 2D top view and view at an inclination angle of ~70 degree, respectively. We observe from Figure 4.5 (a) and (b) that the as-synthesized p-SiNWs are vertically aligned with high aspect-ratio over large area scale. As measured with HRSEM, the diameter of p-SiNWs is in the range of ~100–500 nm. Note that the measured diameter of the SiNWs under study is larger than that grown by MACE method reported by Rasool *et al*. [Rasool *et al.* (2015)].

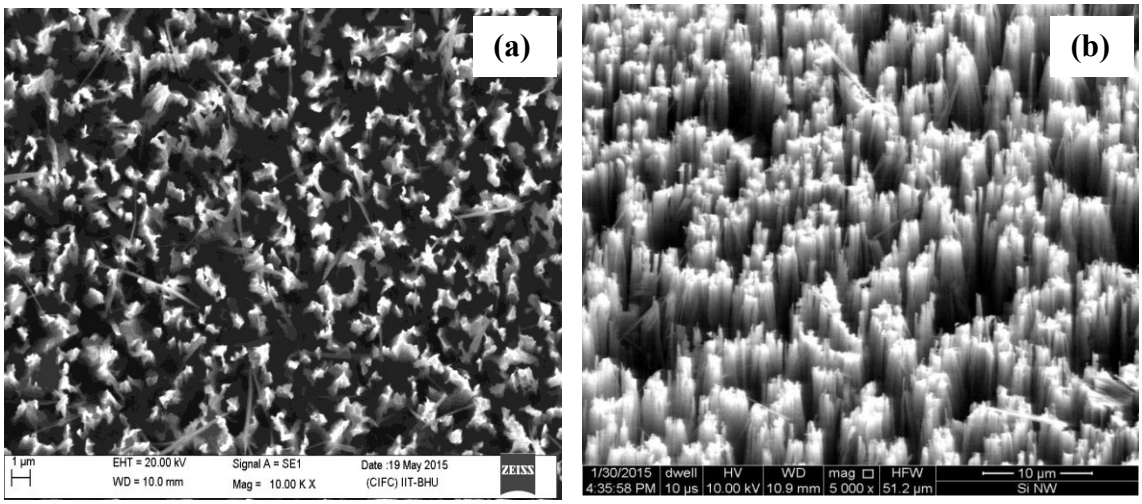

Figure 4.5: (a) HRSEM 2D images of the p-SiNW arrays observed from the (a) Top surface (b) inclination angle of ~70 degree.

(b) Surface morphology study by AFM Results

The 2D and 3D AFM images of the as-grown p-SiNWs are shown in Figure 4.6 (a) and (b). The AFM uses a SiN tip to record images in semi-contact mode with a scanning rate of 0.5 Hz. The scan size or sampling area of 30 μm× 30 μm was recorded after several scans. The AFM images shown in Figure 4.6 (a) and (b) demonstrate the vertically aligned and uniformly distributed p-SiNWs over the complete sample area. To qualitatively analyze the surface morphology of the SiNWs under study, various surface dependent parameters such as surface roughness, peak-to-peak spacing, root mean square (rms) roughness, average grain size and grain length are measured using Nova PX (AFM software) which are listed in Table 4.1. The observed values of peak-to-peak spacing, root mean square, roughness average, average grains size, and grains length are ~1227.40 nm, ~157.60 nm, ~127.33 nm, ~422 nm and ~657 nm, respectively. The obtained values of grains size and grains length using AFM measurement are observed to be in close approximation to the HRSEM results as discussed earlier.

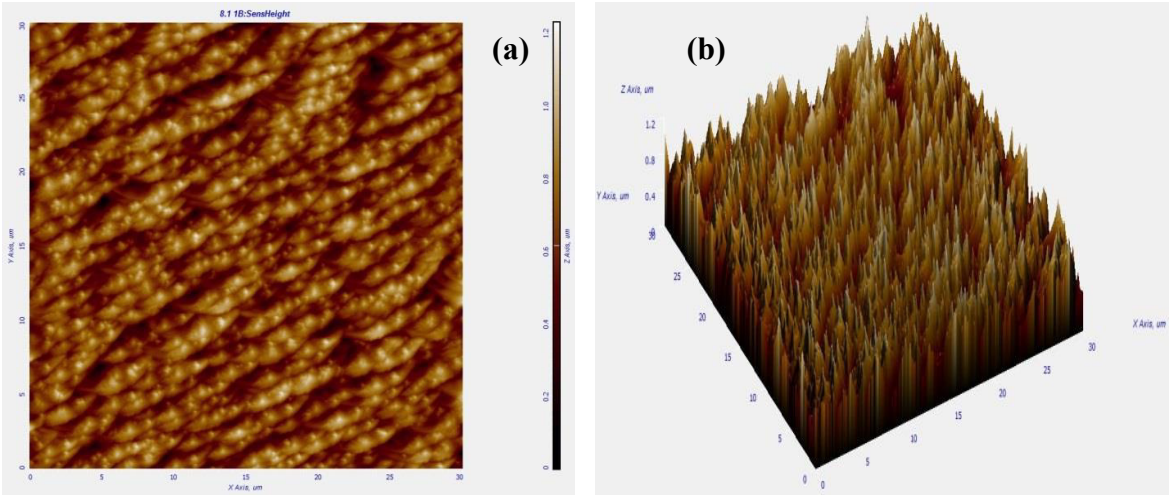

Figure 4.6: (a) 2D and (b) 3D AFM images of as-grown SiNWs synthesized using two-step EMDE Technique.

Table 4.1: AFM derived parameters for as-grown p-SiNWs.

Parameters	**Only p-SiNWs**
Sampling area	30×30 µm
Peak-to-peak spacing	1227.405 nm
Root mean square	157.604 nm
Roughness average	127.332 nm
Average grains size	0.422 µm
Grains length	0.657 µm

(c) Energy dispersive X-ray analysis

The Energy Dispersive X-ray Spectroscopy or analysis (EDS) corresponding to the p-SiNW arrays has been shown in Figure 4.7. Regardless of using chemical etching approach we observed single peak of Si in measured EDS spectra which indicates the absence of any impurities in our fabricated SiNWs. Further the inset table of Figure 4.7 illustrates the weight % and atomic % of element present in the sample.

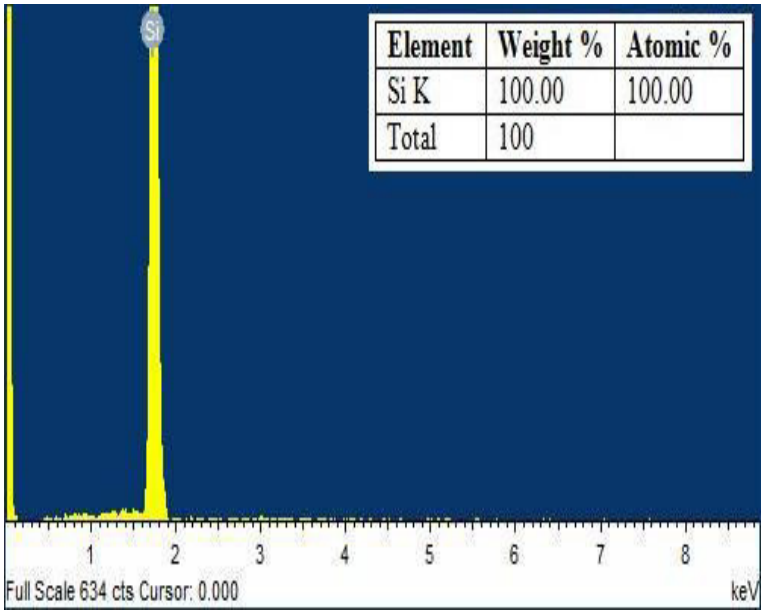

Figure 4.7: EDS spectra of p-SiNW arrays. Inset table illustrates the detail of element present.

(d) Crystallographic Orientation by XRD analysis

Figure 4.8 shows the XRD spectra of as-fabricated p-SiNW arrays. The XRD spectrum confirms single crystalline nature with preferred growth direction in the (400) plane at 2θ ≈69.0°. Thus our fabricated SiNWs have excellent crystalline quality. The XRD pattern is matched with the standard JCPDS PDF having data card no.: 00-001-0787 [Qian *et al.* (2015)].

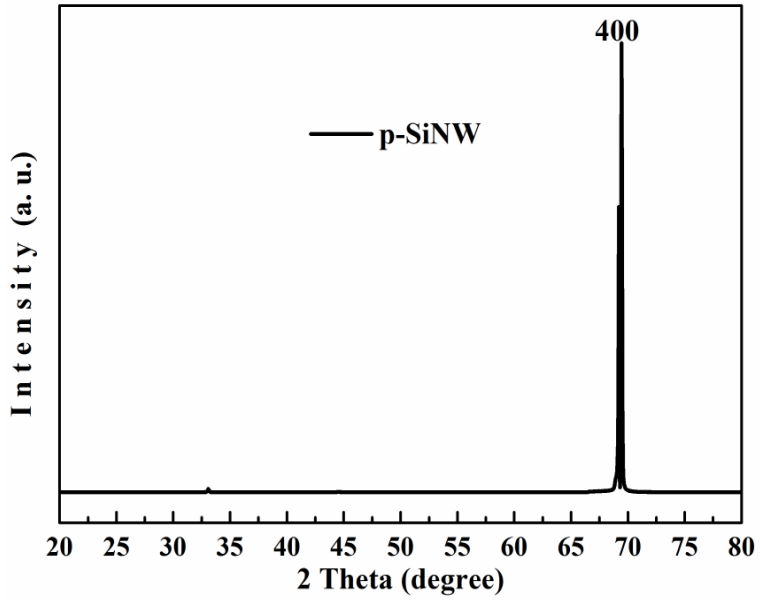

Figure 4.8: XRD spectra of as-fabricated p-SiNW arrays.

4.3.1.2 Optical Characterization of SiNWs

(a) Reflectance of pristine Si and as-fabricated SiNW arrays

Figure 4.9 (a) and (b) compares the reflectance spectra of pristine (bulk) Si wafer and as-grown SiNW arrays under study. It is observed from Figure 4.9 (a) that the reflectance of the pristine silicon substrate is more than 50 % in the UV region while it is larger than 30 % in the visible and IR regions due to its polished surface and high refractive index [Hung *et al.* (2011)]. The reflectance in ~300–850 nm includes the UV

and Visible regions which are important primarily for solar cell applications [Ozdemir *et al.* 2011), Man (2017)]. However, it is observed from Figure 4.9 (b) that the surface of SiNW arrays covering p-Si substrate shows a drastic reduction (<0.3 %) in reflection for ~300–850 nm wavelength as compared to the spectra shown in Figure 4.9 (a). It demonstrates that SiNWs have excellent antireflection property over the wide spectral region ranging from UV to NIR wavelengths. The significant reduction in the reflectance is attributed to the larger surface-to-volume ratio of the SiNWs than the bulk-Si which enhances the scattering effect to trap the incident light within the individual nanowires [Salman *et al.* (2012)]. The low reflectance (i.e. high absorption) of light in the SiNWs can be explored for Si based solar cell and UV detection applications.

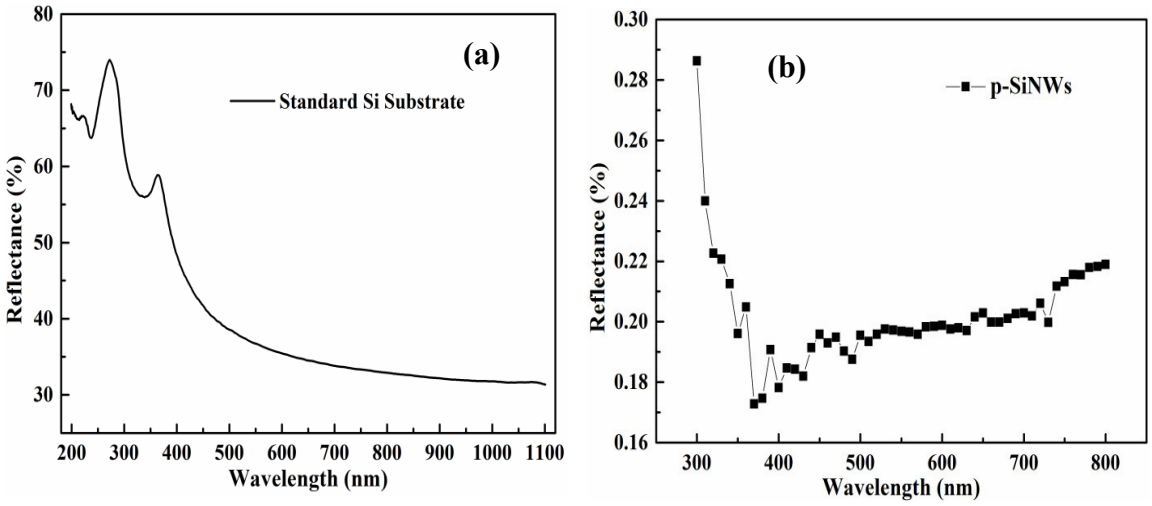

Figure 4.9: Optical Reflectance Spectra of (a) pristine Si wafer (b) as-fabricated p-SiNWs.

(b) Raman spectrum of as-fabricated SiNWs

The Raman spectrum of as-grown SiNWs arrays by the EMDE method with one hour etching duration is shown in Figure 4.10. The Raman measurement set-up (Renishaw,

Model: RM 1000) used for our study includes Ar_+ laser excitation source (with spectral resolution of ~1 cm^{-1}) of 514.5 nm with about 5 mW output power. It may be mentioned that the Raman spectra depends on the excitation wavelength, temperature and dimensions of nanowire [Piscanec *et al.* (2003), Hazra and Jit (2013)]. Figure 4.10 shows two distinct peaks at wave numbers ~297 cm^{-1} and ~520 cm^{-1} corresponding to the second and first order transverse optical phonon mode i.e. 2TO and TO, respectively [Iatsunskyi *et al.* (2014)]. Another significant and broad peak is ranging from ~936 cm^{-1} to ~974 cm^{-1} wave numbers which is attributed to the second order transverse acoustic mode (2TA) where the broadening is attributed to the diameter variation of the NWs [Quiroga-González *et al.* (2014)]. Further two weak peaks at ~604 cm^{-1} and ~423 cm^{-1} may be related to quantum confinement effect of Si [Liu *et al.* (2004)].

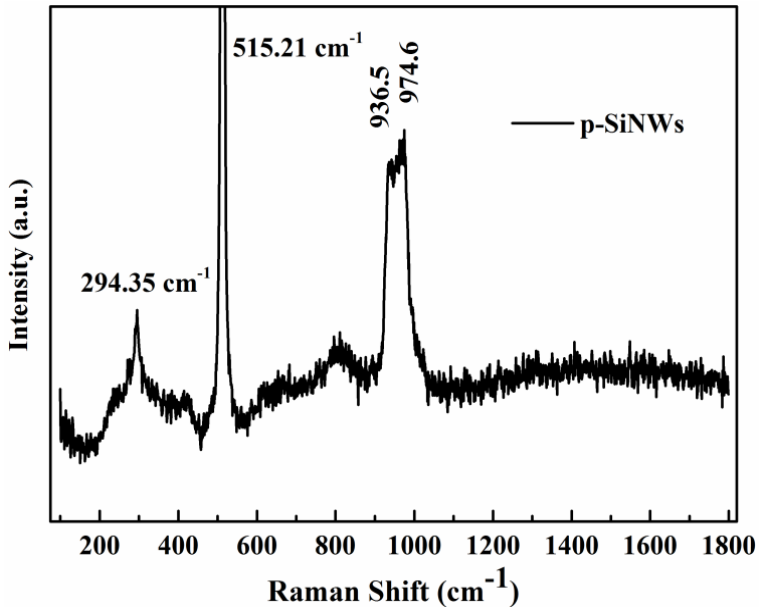

Figure 4.10: Raman spectra of as-prepared SiNWs sample.

4.3.2 Characterization of SiNWs/TiO_2 Heterojunctions

After understanding the properties of as grown p-SiNWs we will now discuss the characterization of n-TiO_2 capped p-SiNWs or in other words p-SiNWs/n-TiO_2

Heterojunctions, where n-TiO_2 have been deposited over p-SiNWs using two methods namely EBE and SG with spin coating.

4.3.2.1 Surface Morphology Characterization

(a) Surface morphology study by SEM

The Scanning Electron Microscopy (SEM) images (Carl Zeiss Microscopy Ltd., UK) of two different samples (grown using EBE and SG method) comprising TiO_2 capped p-SiNWs have been shown in Figure 4.11 and Figure 4.12, respectively. As measured with SEM, the diameter of p-SiNWs is in the range of ~100–500 nm for samples containing only p-SiNWs which is increased to ~620–800 nm after TiO_2 TF deposition as observed in Figure 4.11 and Figure 4.12, respectively.

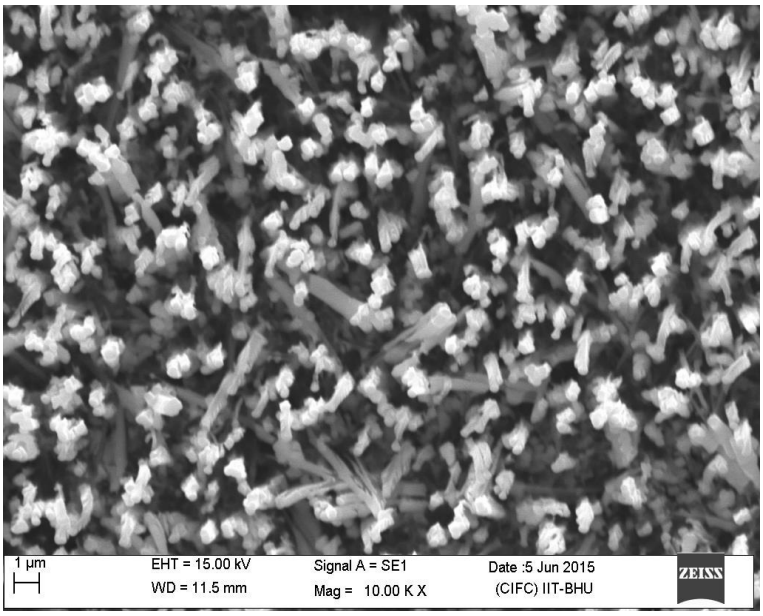

Figure 4.11: Top surface SEM image of TiO_2 capped p-SiNW arrays grown by EBE method.

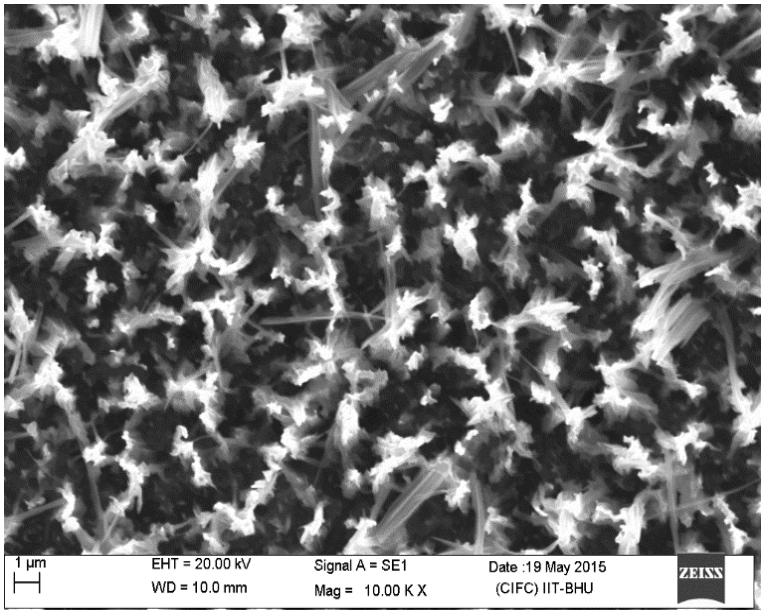

Figure 4.12: Top surface SEM image of TiO_2 capped p-SiNW arrays grown by SG method.

(b) Surface morphology study of the TiO_2 capped SiNWs by AFM

The 2D and 3D surface topographical analysis of the n-TiO_2 capped p-SiNWs have been studied by using AFM (NT-MDT, Model No. NTEGRA Prima) images shown in Figure 4.13 and Figure 4.14 for the n-TiO_2 films deposited on the SiNWs by EBE and SG methods, respectively. Semi-contact mode with SiN tip was used for the image scanning in AFM system. Other parameters of the SiN probe used in our measurement include the following: resonance frequency =255 kHz; elastic constant =11.5 N/m; tip radius ≈10–20 nm; length =100 mm; thickness =2.3 mm; and width =35 mm. The detailed analyses of the AFM images and some surface dependent parameters are listed in Table 4.2. By comparing the AFM images of Figure 4.13 and Figure 4.14 with the AFM image of bare SiNWs sample considered earlier in Figure 4.6, we can easily observe that the surface topography of the SiNWs is modified after the TiO_2 film deposition via EBE and SG methods.

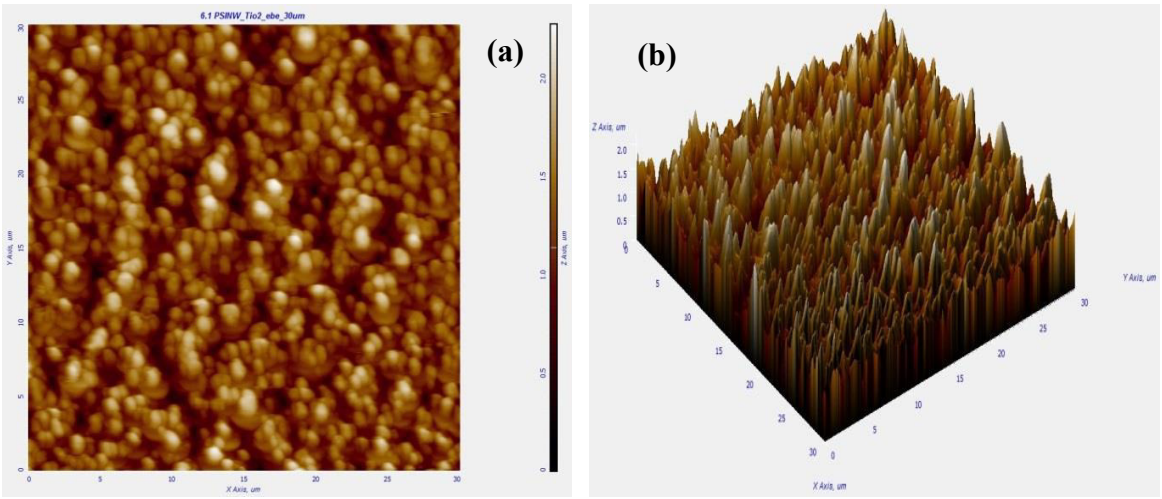

Figure 4.13: (a) 2D **(b)** 3D AFM image of the TiO_2 capped p-SiNW arrays grown by EBE method.

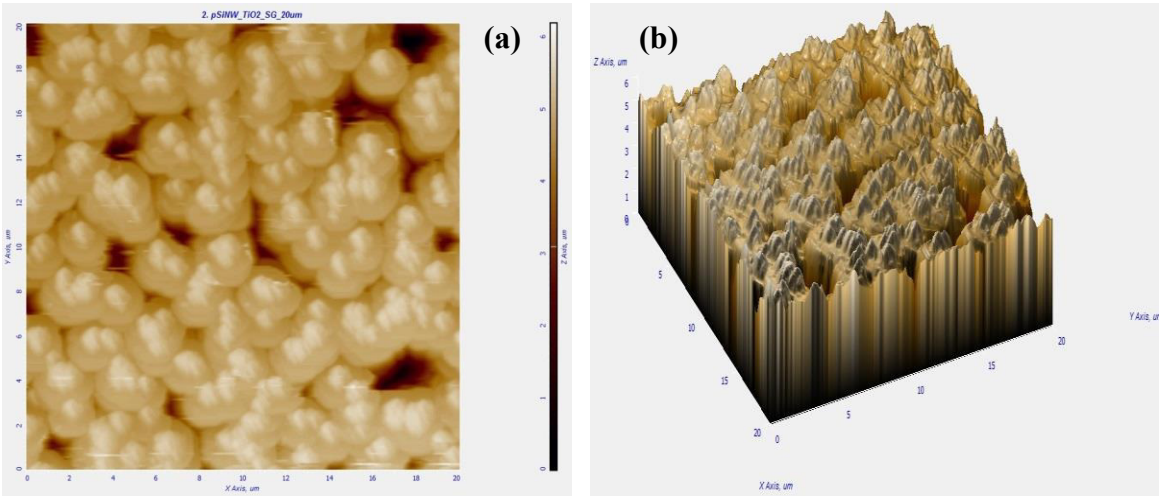

Figure 4.14: (a) 2D **(b)** 3D AFM image of the TiO_2 capped p-SiNW arrays grown by SG method.

Table 4.2: Comparison of AFM Derived Parameters for two deposition techniques under consideration.

Parameters	**SG derived sample**	**EBE derived sample**
Peak-to-peak spacing (µm)	5.594	2.266
Root mean square (µm)	0.595	0.295
Roughness average (µm)	0.375	0.233
Average grains size (µm)	0.553	0.684
Grains length (µm)	0.880	1.031

(c) Energy Dispersive X-ray Spectroscopy

The Energy Dispersive X-ray Spectroscopy (EDS) corresponding to the core-shell p-SiNW/TiO_2 heterojunctions under investigation has been presented in Figure 4.15 (a) and (b). The EDS spectra for samples with core-shell p-SiNW/TiO_2 heterojunctions fabricated using EBE and SG deposition techniques clearly confirm the presence of TiO_2 on the surface as well as in-between the SiNWs. This confirmation is assured in terms of the peaks corresponding to Ti and O elements present from end to end in both the samples. Specifically for the EBE derived sample the average weight % of Ti:O ratio was 26.9:40.98, whereas for the SG derived sample its value is 11.44:27.76. The above mentioned values of average weight % indicate very good chemical stoichiometry of TiO_2 over p-SiNW arrays in both the samples under study. As shown in Figure 4.15 (a) and (b) the peak corresponding to Si is intense and leading due to the bulk substrate containing p-SiNWs which is Si. Further the elemental composition of each sample in terms of weight % and atomic % is also given in the table provided in the inset of Figure 4.15 (a) and (b), respectively.

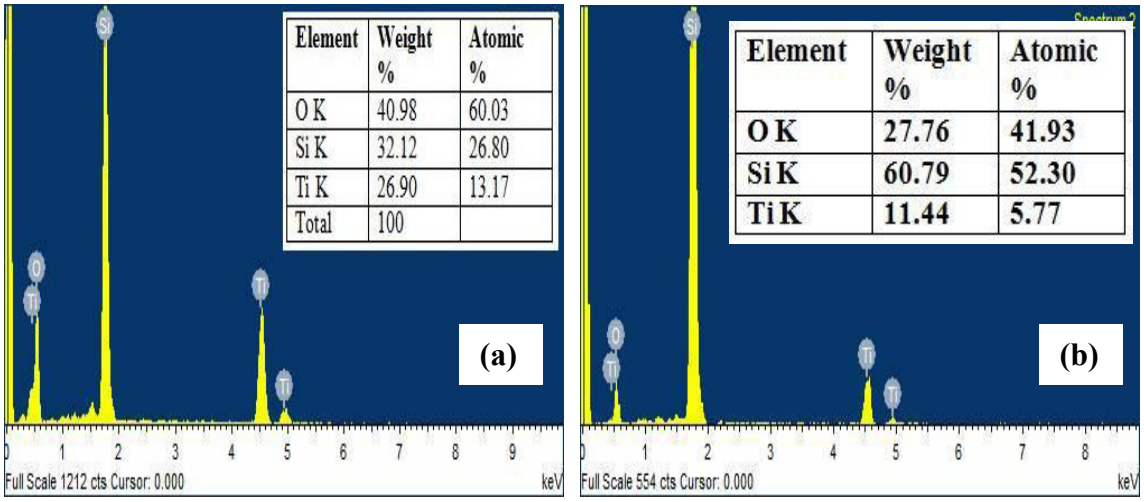

Figure 4.15: EDS spectra of the TiO_2 capped p-SiNW arrays prepared by (a) EBE method (b) SG method. Inset tables illustrate the details of the elements present.

(d) Crystallographic Orientation by XRD analysis

The crystalline structure of the as-synthesized n-TiO_2 capped p-SiNW arrays have been investigated by the XRD (RIGAKU-Smart XDMAX, PC-20, 18-kW Cu rotating anode, Rigaku, Tokyo) spectra shown in Figure 4.16 and Figure 4.18 for the EBE and SG based TiO_2 films, respectively. It may be mentioned that a variety of factors including the instrumental effects, crystallite size, inhomogeneous strain and crystal lattice imperfections can contribute to the width of a diffraction peak. The dislocations, stacking faults, twinning, microstresses, grain boundaries, sub-boundaries, coherency strain, chemical heterogeneities, and crystallite smallness can also contribute to the peak broadening. For a better understanding, we have discussed two techniques for the analysis of measured XRD spectra. In the first analysis, we have used the Debye-Sherrer method [Zhu *et al.* (2017)] in which an ideal situation is assumed by neglecting all of the above mentioned effects on the peak broadening. In other words, the peak width is assumed to be solely dependent on the crystallite size in the Debye-Sherrer analysis. On the other hand, we have also analyzed the XRD spectra by a second approach called Williamson–Hall method [Akgul *et al.* (2015-b)]. The analyses of the XRD spectra by the above two methods have been demonstrated in the following subsections.

(i) XRD analysis for EBE derived TiO_2 capped p-SiNW arrays

θ–2θ XRD pattern for the EBE derived p-SiNW/n-TiO_2 core-shell heterojunction is illustrated in Figure 4.16. The XRD pattern shows the dominant diffractions from anatase phase of n-TiO_2 (JCPDS Card No.: 89-4921) and Silicon (JCPDS Card No.: 00-001-0787) [Qian *et al.* (2015)]. Thus, in our EBE derived samples the anatase phase of TiO_2 is prominent among the known phases of TiO_2 (i.e. anatase, brookite and rutile). In

Figure 4.16 the indexed peaks at 2θ ≈25.31˚, 37.80˚, 48.04˚, 51.96˚, 53.89˚, 55.06˚, 62.69˚ and 68.77˚ correspond to the reflections from (101), (004), (200), (202), (105), (211), (204) and (116) crystal planes of anatase TiO_2 [Thanigainathan and Paramasivan (2012)], whereas additional peaks at ≈28.49˚, 47.05˚ and 56.03˚ correspond to (111), (220) and (311) crystal planes of silicon, respectively [Qian *et al.* (2015)]. Clearly, the XRD spectrum indicates the formation of polycrystalline anatase phase n-TiO_2 with (101) as the dominant diffraction peak.

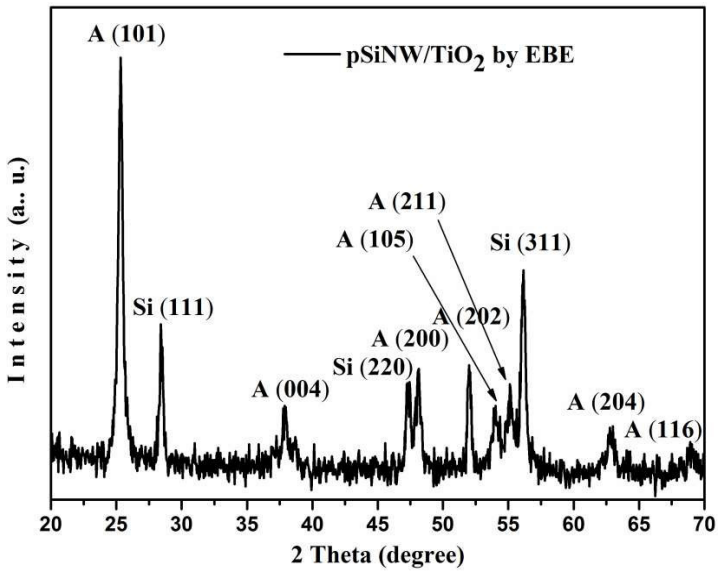

Figure 4.16: θ-2θ XRD spectrum of as-prepared n-TiO_2 film on p-SiNW arrays for the EBE derived sample.

(a) Debye-Sherrer Method: The crystalline size of the as deposited n-TiO_2 TF over p-SiNW arrays has been calculated by Debye-Sherrer formula [Somvanshi and Jit (2014)] as mentioned below:

$$D = \frac{k\lambda}{\beta \cos\theta} = 13.394\,\text{nm} \tag{4.6}$$

where, k is a dimensionless shape factor with a typical value of about ~0.9, θ is the Bragg angle and β is the full width at half maximum (FWHM). The anatase crystallite

size estimated from the FWHM of single dominant A (101) diffraction peak was almost ~13.394 nm. The crystallite size of 13.3194 nm obtained from the Debye-Sheerer formula thus does not provide the actual average value of the size but the lower bound on the crystallite size.

(b) Williamson–Hall method: As per the Williamson–Hall technique [Akgul *et al.* (2015-a)], the relation between the average crystallite size and micro-strain can be expressed as follows [Akgul *et al.* (2015-b)]:

$$\beta\left(\frac{\cos\theta}{\lambda}\right)=\frac{1}{D^2}+\varepsilon\left(\frac{\sin\theta}{\lambda}\right) \tag{4.7}$$

where, D is the average crystallite size, ε is the effective lattice strain, λ is X-ray wavelength, β is the FWHM of the diffraction peaks (in radians), and θ is the Bragg angle of the analyzed peak. In this technique all the diffraction peaks from XRD spectrum (Figure 4.16) were considered to plot β cos θ/λ versus sin θ/λ as shown in Figure 4.17.

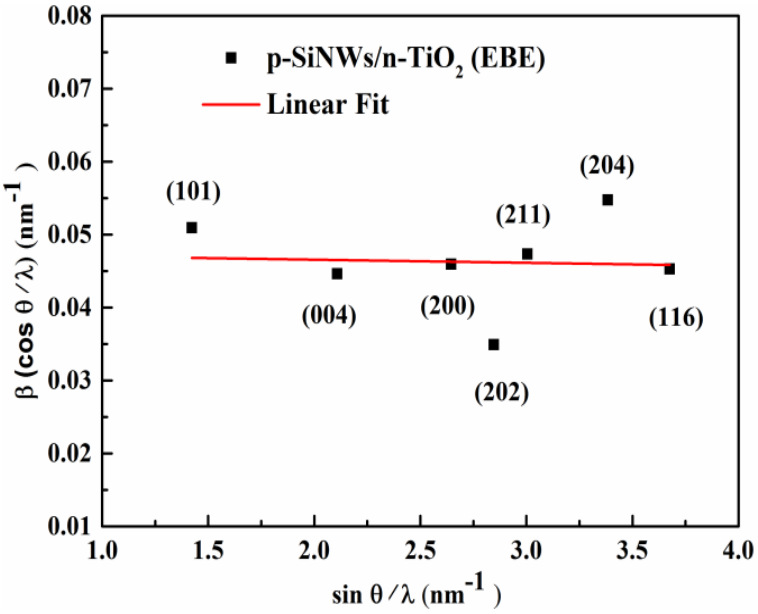

Figure 4.17: Williamson–Hall plot for TiO_2 deposited onto SiNW arrays by EBE method. The red straight line represents the linear fitting of the experimental data.

The mean value of crystallite size ~21 nm is estimated from the inverse of linear fit to $\beta \cos \theta/\lambda$ axis (Figure 4.17). It may be noted that the mean value of the crystallite size estimated from the Williamson–Hall method (~21 nm) is slightly larger than that estimated from the Debye-Scherrer formula (i.e. ~13.3194 nm). The above observations are in good agreement with the theory described in Ref. [Akgul *et al.* (2015-b)].

(ii) XRD analysis for SG derived TiO_2 capped p-SiNW arrays

Figure 4.18 displays the XRD pattern observed for an annealed n-TiO_2 film on p-SiNW arrays sample prepared by using SG method. XRD spectrum demonstrates different peaks corresponding to the crystalline phases of TiO_2 and Si. Different characteristic peaks for n-TiO_2 are corresponding to the polycrystalline nature of as deposited n-TiO_2. XRD spectra for n-TiO_2 exhibits dominant diffraction peaks from anatase phase, while the single weak indexed peak at $2\theta \approx 55.1^{\circ}$ corresponds to the reflections from (211) crystal planes of brookite phase TiO_2. As in accordance with the standard JCPDS file no. 89-4921 [Thanigainathan and Paramasivan (2012)], the diffraction peaks at $2\theta \approx 25.2°$, 37.7°, 44.5°, 48.0°, 52.0°, 62.7°, 53.9°, 76.4°, and 74.9° correspond to the reflections from (101), (004), (221), (200), (202), (204), (105), (301), and (215) crystal planes of anatase TiO_2. Further additional peaks at ≈28.4°, 47.3° and 56.0° correspond to (111), (220), (311) crystal planes of silicon (JCPDS Card No. 00-001-0787 [Qian *et al.* (2015)]).

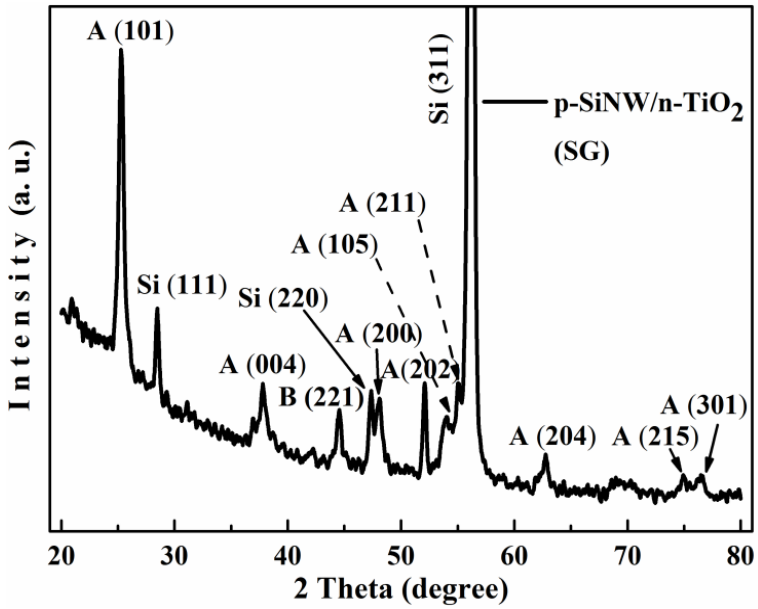

Figure 4.18: θ-2θ XRD spectrum of n-TiO_2 film on p-SiNW arrays for the SG derived sample.

(a) Debye-Sheerer Method: Using the FWHM of single dominant A (101) diffraction peak of Figure 4.18 and Eq. (4.6) we can estimate the crystalline size of as prepared n-TiO_2/p-SiNWs using Debye-Sheerer formula [Somvanshi and Jit (2014)]. The FWHM for A (101) indexed peak is ~14.2241°. The anatase crystallite size estimated for the SG based device is ~14.2241 nm. The crystallite size of ~14.2241 nm obtained from the Debye-Sheerer formula, thus, does not provide the actual average value of the crystallite size but the lower bound on the crystallite size.

(b) Williamson–Hall method: As per the Williamson–Hall method [Akgul *et al.* (2015-a)], all the diffraction peaks of XRD pattern shown in Figure 4.18 are considered to plot the $\beta \cos\theta/\lambda$ versus $\sin\theta/\lambda$ graph which is shown in Figure 4.19.

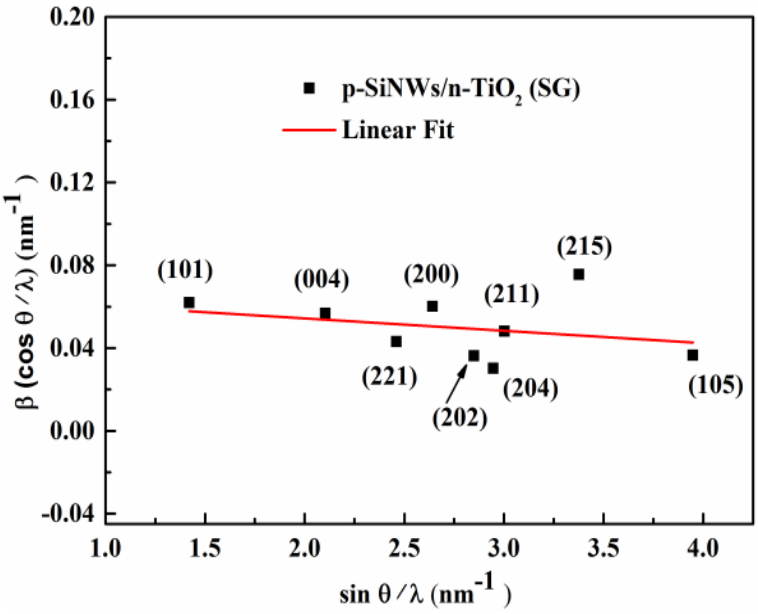

Figure 4.19: Williamson–Hall plot for TiO_2 deposited onto SiNW arrays by SG method. The red straight line represents the linear fitting of the experimental data.

Accordingly, the crystallite size of ~16.666 nm is estimated from the inverse of linear fit to β cos θ/λ axis as shown in the Figure 4.19. Again, the estimated value of ~16.666 nm from this Williamson–Hall method is observed to be slightly greater than that estimated from the Debye-Scherrer formula i.e. ~14.2241 nm, as discussed for the EBE based TiO_2 films. Table 4.3 summarizes the comparison of Debye-Sheerer and Williamson–Hall analyses based on XRD results.

Table 4.3: Comparison of Debye-Sheerer and Williamson–Hall derived XRD analyses results.

XRD Method	***SG based sample***	***EBE based sample***
Debye-Scherrer	14.224 nm	13.394 nm
Williamson–Hall	16.666 nm	21.088 nm

4.3.2.2 Optical Characterizations of SiNW/TiO_2 Heterojunctions

The optical Reflectance and Transmittance analyses for the TiO_2 films grown by EBE and SG methods have already been discussed in Chapter-2 under Section 2.4.2.2.

(a) UV-Vis Measurement of TiO_2 film under Consideration

The UV-Vis Measurements for the TiO_2 films grown by EBE and SG methods have already been discussed in Chapter-2 under Section 2.4.2.2. The key point is that the band gap of EBE and SG based TiO_2 TFs are obtained as ~3.1 eV and ~3.3 eV, respectively.

(b) Raman Characterization of SiNW/TiO_2 Heterojunctions

Raman spectrometer from the Renishaw, Model: RM 1000 was used to record the Micro-Raman spectra having a spectral resolution of 1 cm^{-1} with grating of 2400 grooves/mm at 50 μ slit opening. The excitation source of Ar_+ laser has a wavelength of 514.5 nm with output power of 5 mW. The recorded Raman spectra for EBE and SG based samples are plotted in Figure 4.20. The existence of six Raman active fundamental modes at the following values of wavenumber 144 cm^{-1} (Eg), 197 cm^{-1} (Eg), 397 cm^{-1} (B1g), 518 cm^{-1} (A1g + B1g) and 640 cm^{-1} (Eg) confirms the anatase phase of the TiO_2 film [Chen and Mao, (2007), Vishwas *et al.* (2012)]. Out of six Raman active fundamental modes, four modes at ~145 cm^{-1} (Eg), ~197 cm^{-1} (Eg), ~398 cm^{-1} (B1g) and ~639 cm^{-1} (Eg) were observed for both the samples prepared by using EBE and SG deposition methods for the TiO_2 films. The two modes (A1g + B1g) at ~518 cm^{-1} are merged with the significantly strong LO phonon line of Si at ~520 cm^{-1}. Apart from the n-TiO_2 material, we have also observed Raman peaks attributed to silicon substrate as shown by the peaks at ~294 cm^{-1}, ~936 cm^{-1} to ~974 cm^{-1} wave numbers in Figure 4.20. It is to be noted that the Raman band of the SG based sample

shows some shifting in the Eg mode at peak position (~635 cm^{-1}) with a broad peak width possibly due to the particle size effects [Alam and Cameron, (2002), Grover *et al.* (2014)]. In case of EBE based sample, the lowest frequency mode at ~143 cm^{-1} has the most significant intense peak which is close to the single-crystal anatase phase peak at ~144 cm^{-1} [Vishwas *et al.* (2012)]. This indicates that the as-prepared TiO_2 thin film by the EBE method is well crystallized in the anatase structure. The weak fundamental modes at ~448 cm^{-1}, ~619 cm^{-1}, and ~825 cm^{-1} in the SG based samples may signify the presence of TiO_2 rutile phase [Welte *et al.* (2008)]. However, the details of the Raman modes of SiNW arrays at ~294 cm^{-1}, ~936 cm^{-1} to ~974 cm^{-1} wave numbers [Iatsunskyi *et al.* (2014)] in Figure 4.20 have already been discussed earlier.

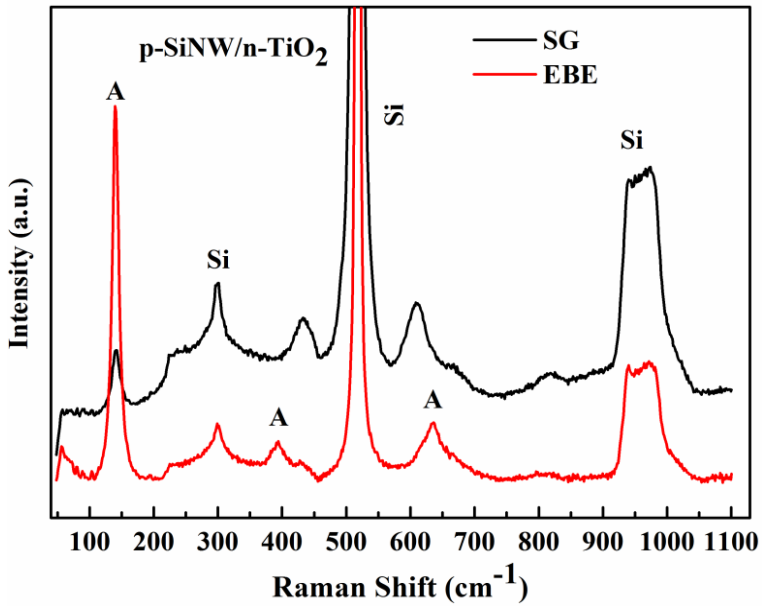

Figure 4.20: Comparative Raman spectra of the TiO_2 capped p-SiNW arrays prepared by EBE and SG methods.

(c) PL Characterization of SiNW/TiO_2 Heterojunctions

Figure 4.21 shows the room temperature Photoluminescence (PL) spectrum measured using Horiba (U.S.A) instrument with Model No: FL321 for as grown samples under

investigation with an excitation wavelength (λ_{Ex}) of ~250 nm. Samples grown by both the deposition techniques i.e. EBE and SG display strong emissions in the UV region with a main peak at λ ≈420.67 nm (~2.947 eV), and weak emissions in the visible region at λ ≈466.49 nm (~2.658 eV), and ≈556.33 nm (~2.228 eV). For samples under consideration emission peak at ~420 nm in Figure 4.21 is attributed to the oxygen related defect emission and the near band edge emission of anatase phase n-TiO_2 TF [Chinnamuthu *et al.* (2012)]. The simultaneous presence of PL peaks in the UV and visible regions indicates the possible applications of the as-fabricated p-SiNW/n-TiO_2 heterostructures for the designing of dual band photodiodes for detecting light in both the UV and visible region [Chinnamuthu *et al.* (2012)]. It is also observed from Figure 4.21 that EBE based heterojunction offers higher emission than that of the SG based sample measured under identical conditions of the PL measurement.

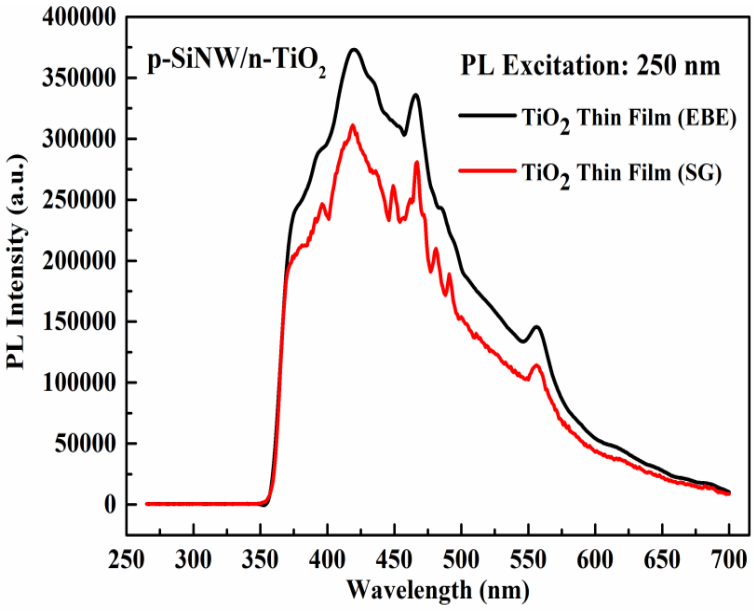

Figure 4.21: Room temperature Photoluminescence spectra of as-grown p-SiNWs/n-TiO_2 samples prepared by using EBE and SG methods.

4.3.2.3 Electrical Characterization of p-SiNWs/n-TiO_2 Heterojunction Diodes

After examining the structural and optical properties of as-prepared p-SiNWs/n-TiO_2 core-shell samples, we now proceed to discuss their electrical characteristics in the following section. The schematic diagram of as fabricated p-SiNWs/n-TiO_2 core-shell heterojunction diode to be used for electrical and photoresponse measurements is shown in Figure 4.22.

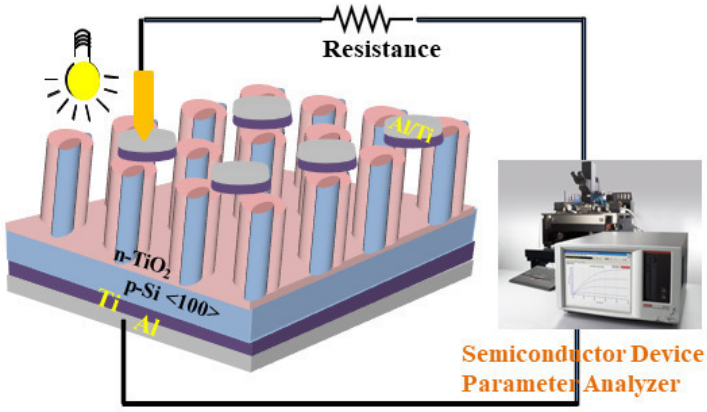

Figure 4.22: Schematic diagram of Al/Ti/p-SiNWs/TiO_2/Ti/Al heterojunction diode prepared by using EBE and SG methods.

(a) Capacitance-Voltage Characteristics

Semiconductor parameter analyzer (Keysight, B1500A) has been used to measure the room temperature Capacitance-Voltage (C-V) characteristics (at ~295 K) of the as-prepared p-SiNWs/n-TiO_2 core-shell heterojunction diodes fabricated by EBE and SG methods as shown in Figures 4.23 and 4.24, respectively. The A^2/C^2 versus applied voltage (V) plots have also been shown in the respective figures. As discussed in Chapter-2, we have measured the room temperature C-V characteristic at 1 MHz frequency. The variation in the C-V characteristics with the change in applied bias voltage in both figures clearly shows the existence of a depletion region at the p-

SiNWs/n-TiO_2 heterojunction interface. Following the similar methodology described in Chapter-2, we have estimated the barrier height, donor concentration and built-in potential of the two p-SiNWs/n-TiO_2 TF heterojunction devices under investigation. The built-in potentials have been estimated as ~0.73 V and ~0.78 V for the EBE and SG based samples. The slope of same linear sections of the A^2/C^2 versus applied voltage (V) plots in Figures 4.23 and 4.24 are used to estimate the average carrier concentration *(N_D)* as ~4.4681×10^{19} cm^{-3} and ~1.0859×10^{19} cm^{-3} for EBE and SG based TiO_2 films in heterostructured diodes under study. The barrier heights for EBE and SG based core-shell heterojunction diodes are ~0.82826 eV and ~0.91427 eV, respectively at room temperature.

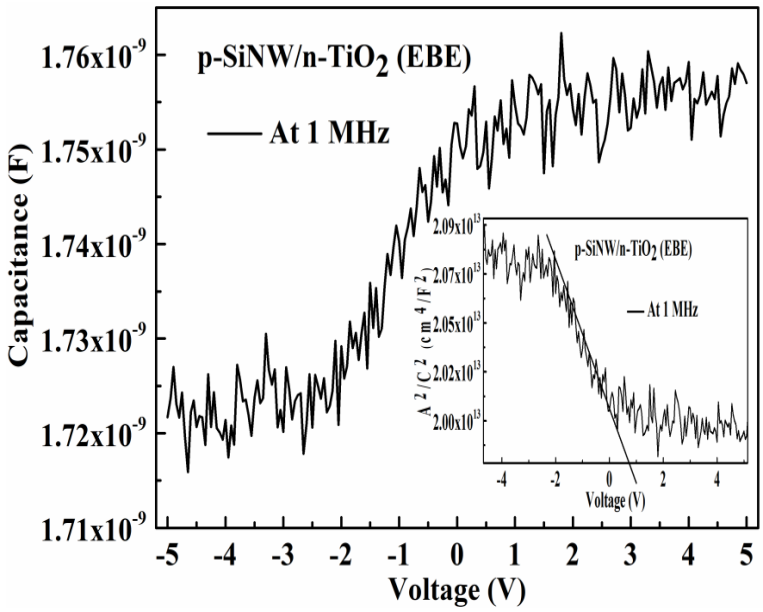

Figure 4.23: C–V characteristics for n-TiO_2/p-SiNWs heterojunction diode fabricated using EBE method. The inset figure illustrates its respective A^2/C^2 versus V plot.

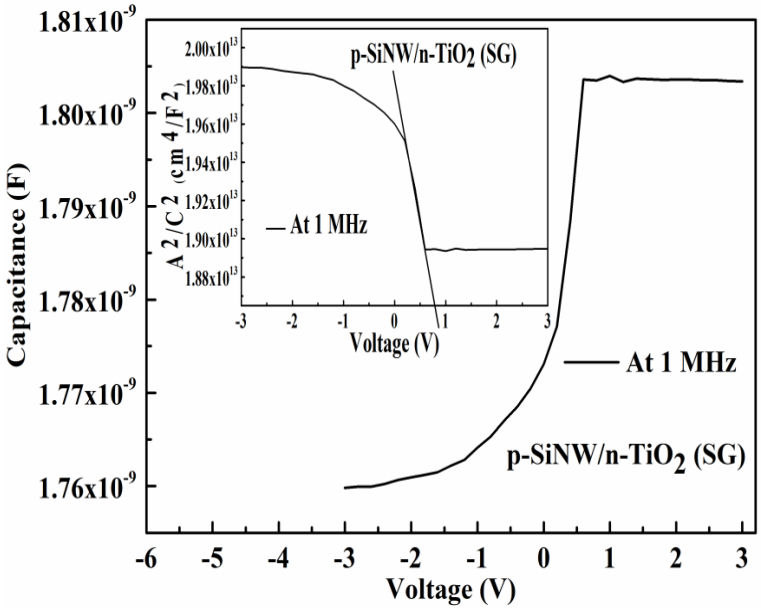

Figure 4.24: C–V characteristics for n-TiO_2/p-SiNWs heterojunction diode fabricated using SG method. The inset figure illustrates its respective A^2/C^2 versus V plot.

(b) Current-Voltage Characteristics of p-SiNW/n-TiO_2 Heterojunction Diodes Under Dark Condition

We now analyze the current-voltage $(I-V)$ characteristics of the as fabricated p-SiNWs/n-TiO_2 heterojunction diodes over bias voltage range of -12 V to +12 V measured by using semiconductor parameter analyzer from Keysight (Model No. B1500A) under dark conditions. Figure 4.25 shows the semi-logarithmic room temperature J-V characteristics for the EBE and SG derived heterojunction diodes under dark environment. The EBE technique based device under consideration shows the excellent rectifying behaviour with rectification ratio (i.e. the ratio of forward bias current to the reverse bias current) (I_F/I_R) of ~519.82 at ±12 V bias which is much larger than that of p-Si/n-TiO_2 heterojunction diode [Selman *et al.* (2014), Rawat *et al.* (2016)] and p-Cu_2O-shell/n-TiO_2 nanowire-core heterostucture [Tsai *et al.* (2011)]. It is also important to mention that further improved I_F to I_R ratio was observed for the SG

based device (in comparison to EBE derived device) with the value of (I_F/I_R) ~673.25 at ±12 V bias. The above calculated values of rectification ratio (considering both diodes) indicate the formation of a depletion region in between p-SiNWs and n-TiO_2 junction. Figure 4.26 also displays the comparative variation of the rectification ratio with respect to the bias voltage for p-SiNWs/n-TiO_2 heterojunction diodes under consideration. The $I-V$ characteristics of the two heterojunction diodes under study can be described by thermionic emission theory [Sze (1981), Zhang *et al.* (2012-a)]:

$$I = I_0\left\{\exp\left(\frac{qV}{\eta kT}\right)-1\right\} \tag{4.8}$$

$$I_0 = AA^*T^2\exp\left(-\frac{q\phi_{B,eff}}{kT}\right) \tag{4.9}$$

where, all the abbreviations have their standard meanings and are already defined in Chapter-2.

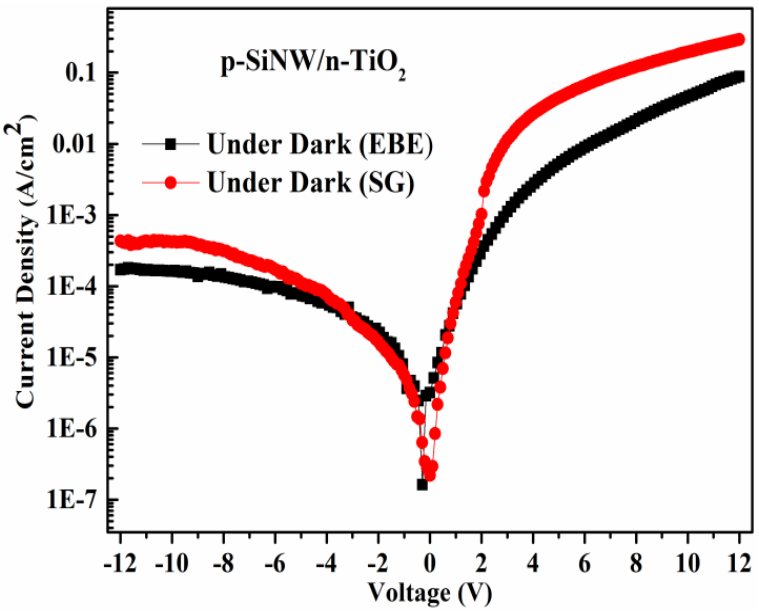

Figure 4.25: Semi-logarithmic room temperature J-V characteristics for the EBE and SG p-SiNW/n-TiO_2 heterojunction diodes under dark environment.

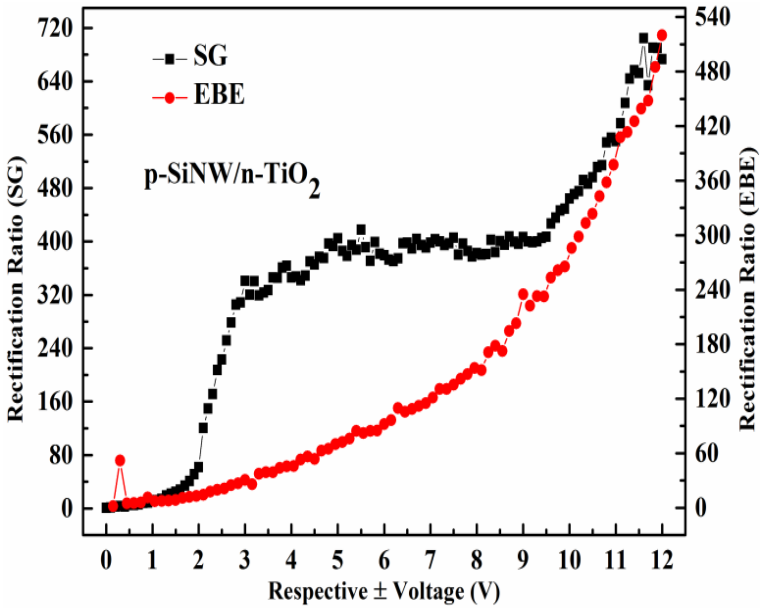

Figure 4.26: Comparative variation of the rectification ratio with respect to the bias voltage for p-SiNWs/n-TiO_2 Heterojunction Diodes under consideration.

The value of I_0 is estimated by extrapolating the linear region of $\ln(I)-V$ plot to zero bias-voltage [Somvanshi and Jit (2014)]. The estimated values of I_0 for the EBE based sample is ~24.836 nA and for the SG based sample ~4.167 nA. Thus SG based device offers slightly lower value of reverse saturation current. The value of effective barrier height at zero bias can be computed by using the following relation [Sze (1981), Somvanshi and Jit (2014)]:

$$\phi_{B,eff} = \left(\frac{kT}{q}\right)\ln\left(\frac{AA^{*}T^{2}}{I_0}\right) \tag{4.10}$$

By using the value of I_0 in Eq. (4.10), $\phi_{B,eff}$ is calculated as ~0.7924 eV for the EBE based p-SiNW/n-TiO_2 heterojunction device and ~0.8379 eV for the SG based p-SiNW/n-TiO_2 heterojunction device. Table 4.4 shows the parameters that were extracted from the semi-logarithmic I-V plot of Figure 4.25 and above mentioned equations. We observed some distinction between the parameter values obtained for the

SG and EBE based devices. High barrier heights have been observed for the SG device together with very low reverse current. But the ideality factor is comparatively higher for the SG based sample.

Table 4.4: Electrical parameters of SiNWs/TiO_2 heterojunction diode Under Dark condition.

Parameters	**SG device**	**EBE device**
On/off ratio at ±12V (Rectification ratio)	673.259	519.82
Saturation current (nA)	4.167	24.836
Ideality factor (η)	6.627	5.498
Barrier height (eV)	0.8379	0.7924

(c) Current-Voltage Characteristics of p-SiNW/n-TiO_2 Heterojunction UV Photodiodes

Now, we will investigate the UV-A detection characteristics of the as fabricated heterojunction diodes at room temperature. For the photo response measurement, we have used the UV source (make: BENCHMARK, India) with an output optical power *(P_{opt})* of ~650 μW (measured by a power meter of model no.: FOMP-101, BENCHMARK, India) at wavelength *(λ)* ~365 nm. Figure 4.27 shows comparative $\ln J - V$ characteristics of p-SiNW/n-TiO_2 heterojunction diodes under dark and UV-A illumination conditions. As per definition of Photodiodes under light illuminated condition, significant increase in the diode current (for two diodes under study) was observed in the reverse bias condition compared to the current under forward bias condition. Different mechanisms such as absorption of the incident light, photo carrier generation, carrier trapping, detrapping, and recombination on the TiO_2 surface are responsible for this significant change [Sze (1981), Selman *et al.* (2014)]. On the other

hand, the distribution of charge carriers inside the p-SiNW/n-TiO_2 heterojunction diodes also play crucial role as briefly explained later. When our fabricated devices are illuminated with UV light, the turn-on voltage (V_{ON}) and barrier height $(\phi_{B,eff})$ are reduced with respect to their corresponding initial values measured under dark condition. For EBE based sample $\Delta\phi_{B,eff}$ ≈0.0164 eV, whereas in case of SG based sample $\Delta\phi_{B,eff}$ ≈0.1795 eV. As discussed in Chapter-1 that the dark current and photocurrent in SiNWs based devices are usually changed with the variation of dimensions for the NWs [Soci *et al.* (2010)]. The contrast ratio or sensitivity defined as the ratio of the photocurrent (I_{ph}) to dark current (I_d) for the photodiodes under consideration and its relevant plot is shown in Figure 4.28. The calculated values of contrast ratio at -11 V bias for EBE and SG based samples are ~113.82 and ~1212.63, respectively. Specifically at -11 V bias SG device offers higher contrast ratio.

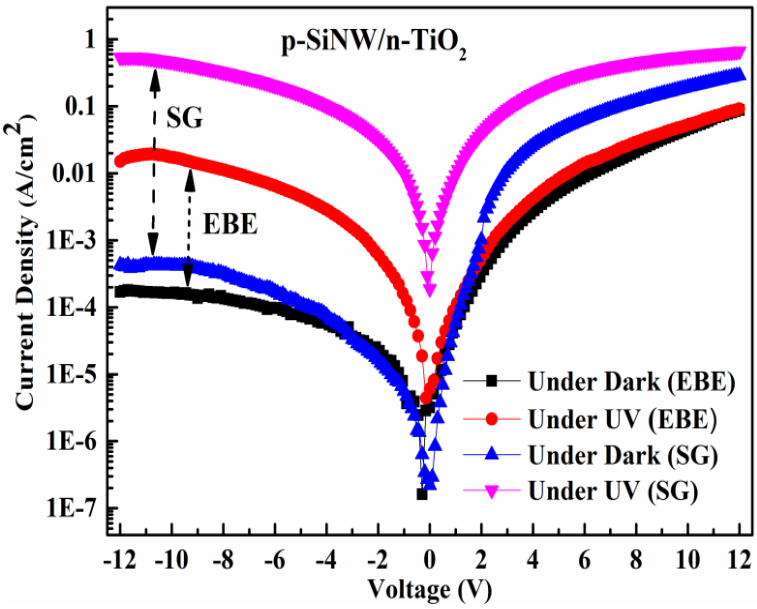

Figure 4.27: Comparative, $\ln J - V$ characteristics of the p-SiNW/n-TiO_2 heterojunction UV photodiodes prepared by using EBE and SG methods.

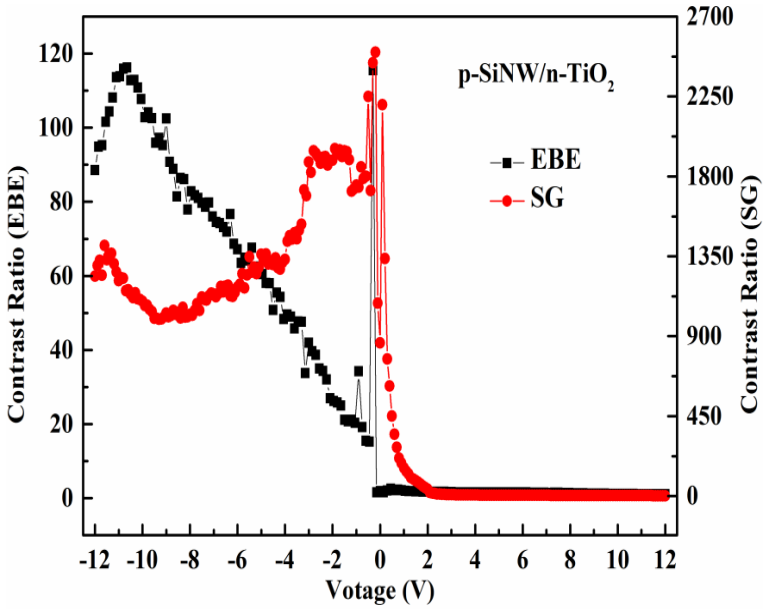

Figure 4.28: Comparative variation of the contrast ratio with respect to applied bias voltage for the p-SiNWs/n-TiO_2 heterojunction diodes under consideration.

Further in comparison to the reported literature our estimated values of contrast ratio (considering both devices) are better than the reported results for p-Cu_2O-shell/n-TiO_2 NW-core heterostucture [Tsai *et al.* (2011)], p-Si/TiO_2 NW heterojunction [Sani (2014)], p-Si/TiO_2 TF [Chinnamuthu *et al.* (2012), Rawat *et al.* (2016)] and TiO_2 NW Schottky diodes [Chinnamuthu *et al.* (2012)]. The estimated values of rectification ratio and contrast ratio suggest that fabricated p-SiNW/n-TiO_2 heterojunction diode structure can be a good candidate for UV detection applications. Other supporting reasons include that the anatase phase TiO_2 and SiNWs are hydrophilic in nature [Rasool *et al.* (2015)]. Thus, the p-SiNWs have the tendency to attract hydrophilic contents $\left(O^-, O_2^-, OH^-\right.$ and $\left.H_2O\right)$ from TiO_2 and form acceptor like states at p-SiNWs surface thereby resulting in a good bonding and an increase in the electrical current as shown in Figure 4.27.

Now, we will estimate the key device performance parameters such as the Responsivity (R_{UV}), External Quantum Efficiency (EQE), Gain, Bias dependent specific detectivity (D), and Resistance-Area product (RA) for the UV photodiodes prepared using EBE and SG methods. The responsivity determines the sensitivity of diode to the incident light input and is calculated by using the following relation [Selman *et al.* (2014)]:

$$R_{UV} = \frac{I_{ph}}{P_{opt}} \tag{4.11}$$

where, P_{opt} is the incident optical power. The calculated values of responsivity (R_{UV}) for EBE and SG method based photodetectors are ~0.23353 A/W and ~6.34148 A/W, respectively at a bias voltage of -11 V. The significantly higher value of responsivity (R_{UV}) for SG based photodetector indicates its superiority and the photo-multiplication phenomena. The significant changes in responsivity (R_{UV}) indicates that the deposition technique is a key parameter in determining the optical properties. Comparing both the above calculated results with reported literature we note that the responsivities of our fabricated devices are better than other photodiodes based on SiNWs hybrid device [Rasool *et al.* (2012)], p-Si/TiO_2 heterojunctions [Selman *et al.* (2014), Sani (2014), Mazhir *et al.* (2015)], and Schottky diode [Chakrabartty *et al.* (2014)].

Next, EQE is defined as the ratio of photoelectrons produced by the incident photons to the number of incident photons. Note, that EQE doesn't include subsequent photons produced by amplification processes. The calculation of EQE is an alternative way of measuring optical to electrical conversion efficiency in a detector. It is given by the following relation [Sze (1981), Hazra *et al.* (2014-c)]:

$$EQE = \frac{hc}{q\lambda} R_{UV} = \frac{1240 \times R_{UV}}{\lambda(in\ nm)} \tag{4.12}$$

where, c is the velocity of light and $\lambda(nm)$ is the wavelength of incident light.

The EQE of EBE derived p-SiNW/n-TiO_2 heterojunction diode is ~79.337 % at -11 V bias and this value is superior than the reported values of p-Si/TiO_2 based heterojunctions [Mazhir *et al.* (2015)], SiNWs hybrid device [Rasool *et al.* (2012)], and schottky diode [Chakrabartty *et al.* (2014)]. The enhanced *EQE* for the SiNWs devices is attributed to the waveguiding effect [Rasool *et al.* (2012)] when illuminated by light source. The comparative higher responsivity of SG based device signifies the existence of an internal photoconductive gain (photomultiplication). Thus its photoconductive gain *(g)* can be estimated as mentioned below [Soci *et al.* (2007), Huang *et al.* (2010)]:

$$g = \frac{1240 \times R_{UV}}{\lambda(nm) \times EQE} \tag{4.13}$$

where, EQE is external quantum efficiency and $\lambda(nm)$ is the wavelength in nm of the incident UV light. Assuming $EQE = 1$ [Soci *et al.* (2007)], the gain is calculated as ~21.54 at -11 V bias for the SG based device. Our estimated gain for the SG device is higher than reported in literature Ref. [Selman *et al.* (2014)].

Now, we can define the voltage dependent detectivity (D) as [Rasool *et al.* (2012)]:

$$D = R_{UV}\left(\frac{RA}{4kT}\right)^{1/2} \tag{4.14}$$

where, RA is the resistance-area product of the detector which can be acquired from the $\ln J - V$ characteristics as [Hazra *et al.* (2014-c)]:

$$RA = \left(\frac{dJ}{dV}\right)^{-1} \tag{4.15}$$

The estimated values of RA and *D* are ~227963.52 Ω.m^2 and ~8.66462×10^{11} mHz$^{1/2}$W^{-1} at -11 V bias for EBE derived diode. Whereas RA and *D* are ~17.40 Ω.m^2 and

~2.05569 ×10^{11} $mHz^{1/2}W^{-1}$, respectively at -11 V bias for SG derived diode. Further the zero-bias resistance-area product (R_0A) value is obtained as ~9.98004×10^6 Ω.m^2 and ~218.27 Ω.m^2 with respect to EBE and SG diodes. The enhanced detectivities *(D)* are attributed to the desorption of oxygen on the TiO_2 surface [Selman *et al.* (2014)], higher aspect ratio for vertical SiNW arrays and trapping of more number of the incident photons due to more scattering of light inside the n-SiNW structure [Chinnamuthu *et al.* (2012)]. It is observed that both the diodes offers approximately similar values of Detectivity (D) which is better than the reported values for p-SiNW/TiO_2 and SiNWs hybrid device [Rasool *et al.* (2012)], p-Si/TiO_2 based heterojunction [Mazhir *et al.* (2015), Rawat *et al.* (2016)]. Further, our D is also superior to some detectors based on other materials, such as the MoS_2 device [Choi *et al.* (2012)] and p-Si/n-ZnO heterojunction [Hazra *et al.* (2014-c)].

All the above estimated results for two kinds of photodetectors under study are summarized in Table 4.5.

Table 4.5: Comparison of the UV photo detection parameters for two present p-SiNWs/n-TiO_2 heterojunction photodiodes under study.

UV wavelength	365 nm	
Power of incident light	650 µW	
Operating Voltage	-11 V	
Parameters	**SG Device**	**EBE Device**
Contrast ratio	1212.63	113.82
Responsivity [A/W]	6.341	0.233
Barrier height after UV (eV)	0.6584	0.776
Detectivity [$mHz^{1/2}W^{-1}$]	2.055×10^{11}	8.664×10^{11}
Gain/ EQE	21.543	79.337 %
RA products [Ω.m^2]	17.401	227963.52
Zero-bias R_0A [Ω.m^2]	218.270	9.980×10^6

Table 4.6: Comparison of Different UV Detection Parameter For TiO_2 Based UV Detector.

Device structure	I_F/I_R	I_{pd}/I_d	R_{UV} (A/W)	*EQE* (%)	D(mHz$^{1/2}$W^{-1})	Ref.
SiNWs/TiO_2	519.8	113.82	0.23 at -11V	79.3	8.66×10^{11}	our work
SiNW	-	1.30	0.067 at 1V	13.2	5.2×10^{7}	[Rasool *et al.* (2012)]
SiNW/TiO_2	-	2.39	0.8013 at 1V	157	2.44×10^{8}	
p-Si/TiO_2	2.23	290	0.106 at 5V	3.92	-	[Selman *et al.* (2014)]
Hetrostr.	19.76	34.12	-	-	-	[Tsai (2011)]
p-Si/TiO_2	-	-	0.0326 400 nm	11.0	3.261×10^{6}	[Mazhir *et al.* 2015]
Schottky diodes	-	17.90	.05 at-8V	16	-	[Chakrabartty *et al.* (2014)]
p-Si/TiO_2	-	1.5	.034 at -4V	-	-	[Sani (2014)]
p-Si/TiO_2 (by EBE)	237	14.92	-	-	8.62×10^{10}	[Rawat *et al.* 2016]

The improvement in the values of *EQE* and *D* of the present p-SiNWs/n-TiO_2 heterojunctions over the p-Si/n-TiO_2 TF heterojunction discussed in Chapter-2 is attributed to the increase in light absorption efficiency by particle induced light scattering due to the enhanced hydrophilic nature of the surface of p-SiNWs [Niu *et al.* (2004), Chinnamuthu *et al.* (2012)]. In addition Table 4.6 shows some comparative values of our diode performance parameters with other reported results in the literature.

4.3.2.4 Time Response Characteristics

Now we will investigate the transient response for the two types of nanostructured p-SiNWs/n-TiO_2 heterojunction diodes under consideration. We have used the same

measurement setup as used for the measurements of p-Si(bulk)/n-TiO_2 heterojunctions studied in Chapter-2. An UV LED source with ON-OFF light pulse duration of 1 sec. each is incident on the two nanostructured p-SiNWs/n-TiO_2 heterojunction photodiodes operated at a fixed -2 V DC bias. The measured transient responses (i.e. graph between time (sec.) and current (A)) for the EBE and SG based diodes under study are shown in Figure 4.29 (a) and (b), respectively. The estimated average response (rise) time and recovery (fall) time for two diodes are ~32.25 ms and ~37.87 ms for EBE based device and ~29.55 ms and ~32.97 ms, for SG based device, respectively. Thus, the SG based nanostructured p-SiNWs/n-TiO_2 heterojunction diode shows faster response time and recovery time than the EBE based device as well as some other TiO_2 based devices reported in literature [Xue *et al.* (2007), Xie *et al.* (2013), Sani (2014), Chakrabartty *et al.* (2014), Selman and Hassan (2015), Zhang *et al.* (2015-c)].

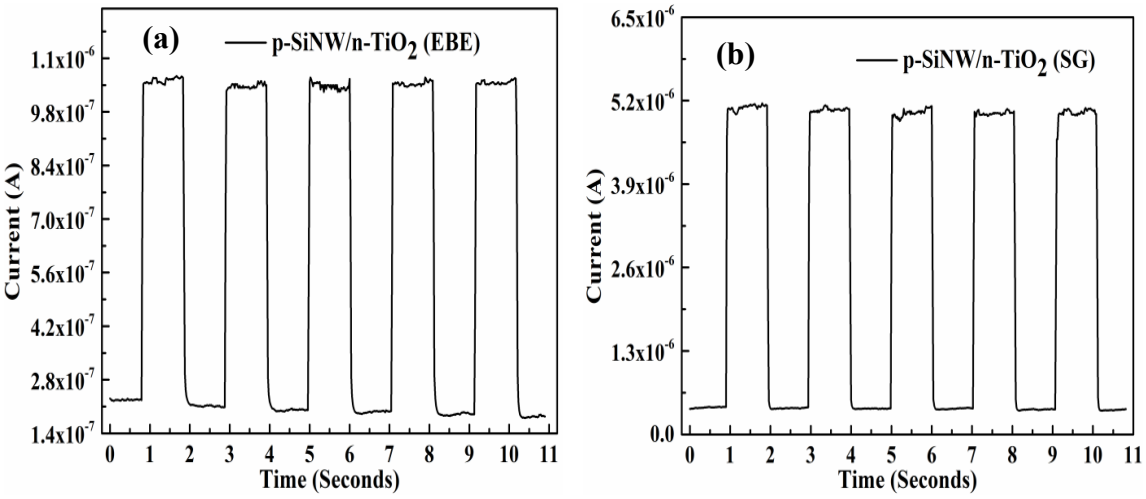

Figure 4.29: Current vs Time characteristics of the heterojunction PDs under dark and UV environment for (a) EBE and (b) SG derived TFs.

4.3.2.5 Energy Band Diagram of n-TiO_2 Thin Film/p-Si Nanowires (NWs) Heterojunction Diode Under UV Illumination

The diameter of synthesized p-SiNW in our work is ~400 nm which is too large to affect the energy bands [Yan *et al.* (2007)]. Thus, the energy-band of p-SiNWs/n-TiO_2 can be assumed to be same as that of p-Si/n-TiO_2 heterojunction diode [Yu *et al.* (2009-a), Yu *et al.* (2009-b)] as shown in Figure 4.30 (a) for equilibrium condition of the junction. The energy band diagram is drawn with the assumption that the oxygen surface charge states are constant during the heterojunction formation.

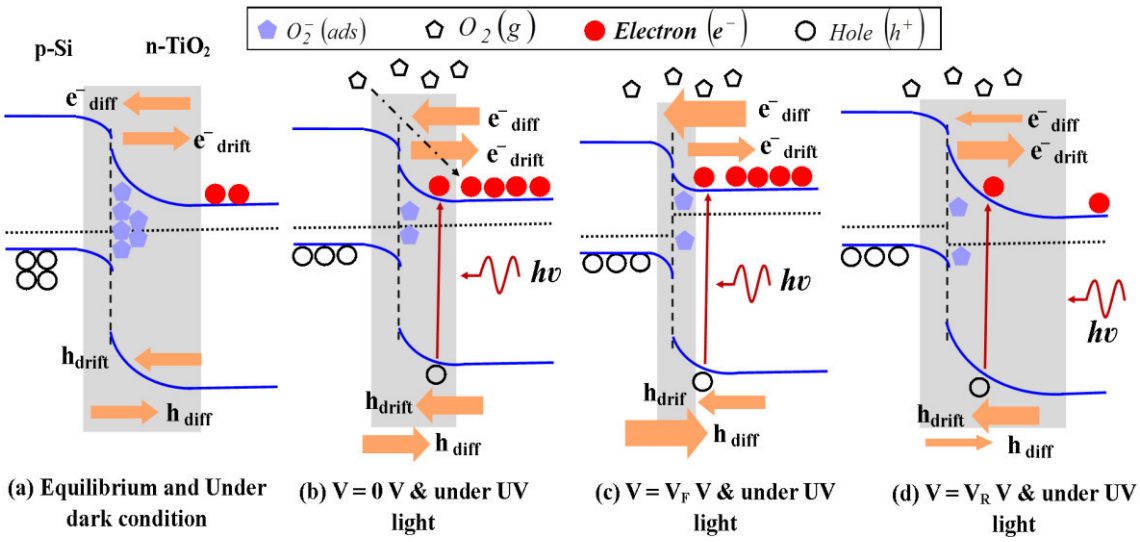

Figure 4.30: Energy band diagram of p-Si and n-TiO_2 heterojunction (a) in equilibrium and under dark condition, (b) at zero bias and under UV light, (c) forward biased and under UV light, (d) reverse biased and under UV light.

Now the UV response under reverse bias can be attributed to the presence of excess oxygen related hole-trap states at the surface of TiO_2 which extends the lifetime of holes by preventing charge-carrier recombination [Chen *et al.* (2015)]. In dark condition, oxygen molecules capture free electrons from n-type TiO_2 and make adsorbed oxygen

$\left(O_2^-(\text{ads})\right)$ i.e $O_2^-(\text{ads})$ at the interface. The oxygen adsorption $\left(O_2(g)+e^- \rightarrow O_2^-(\text{ads})\right)$ results in the formation of a low-conductivity depletion region near the TiO_2 surface. For the diagram shown in Figure 4.30 (b) under illumination, the n-TiO_2 absorbs the UV light of wavelength $h\upsilon \geq E_g$ and generates electron–hole pairs in the depletion region i.e. $\left(h\upsilon \rightarrow h^+ + e^-\right)$. The photo-generated holes are drifted towards TiO_2 surface thereby neutralizing the negatively charged oxygen ions i.e. $\left(h^+ + O_2^-(\text{ads}) \rightarrow O_2(g)\right)$ followed by the release of oxygen atoms from the surface leaving the electrons behind. This is the way by which oxygen is photo-desorbed from the n-TiO_2 surface. The large surface area and trapping mechanism involved in the oxygen adsorption and desorption increases the photo-generated electrons at the surface which, in turn, increases the photo conductivity of TiO_2 film. Since the barrier height does not change under zero-bias condition, the drift and diffusion current components crossing junction are equal and opposite to each other which leads to the zero net current flowing through the heterojunction (see Figure 4.30 (b)). Under forward bias condition of the device shown in Figure 4.30 (c), the volume of the depletion region is reduced which, in turn, reduces the number of photo-generated carries in the depletion region, and hence the photocurrent due to the drifting of photo-generated carriers is also reduced. However, the dark current may be increased due to the increase in diffusion current resulting from the reduction in barrier at the junction under forward bias condition. Under reverse bias condition shown in Figure 4.30 (d), the number of photo-generated carriers in the depletion region is increased due to the increase in the depletion volume. Thus, more number of electrons and holes are drifted towards the p-side and n-side, respectively. This results in the significant increase in the photocurrent while the dark current caused by diffusion is decreased due to increased barrier height

under reverse bias condition.

Assuming the values of electron affinity for n-TiO_2 ~4.1 eV [Chen *et al.* (2015)] and p-Si ~4.05 eV [Majumdar and Banerji (2009)], the respective values of the conduction band offset, $\Delta E_C = \chi_{TiO_2} - \chi_{Si} = 0.05\,\text{eV}$, and valence band offset, $\Delta E_V = E_{g,TiO_2} - E_{g,Si} + \Delta E_C = 2.13\,\text{eV}$, are calculated using Anderson's model [Anderson (1962), Sze (1981), Majumdar and Banerji (2009)]. Clearly, the current transport considered in the present device can be determined predominantly by the flow of electrons.

4.4 Summary and Conclusion

This chapter investigates the electrical and UV-A detection characteristics of p-SiNWs/n-TiO_2 nanostructured heterojunction diodes. The highly oriented, uniform and vertically aligned p-type single crystalline silicon nanowire (SiNW) arrays have been synthesized by the Electroless Metal Deposition and Etching (EMDE) of the bulk p-Si <100> substrates. Two core-shell heterojunction diode structures have been fabricated by depositing the n-TiO_2 films on the p-SiNWs using two different techniques i.e. EBE and SG with spin coating methods. The surface morphology and crystallinity of p-SiNWs and n-TiO_2 capped SiNWs have been characterized by SEM, AFM, EDS and XRD techniques. The SEM measurement shows that the diameter of p-SiNWs is increased from ~100–500 nm to ~620–800 nm when TiO_2 TF is deposited on the SiNWs. The as-deposited TiO_2 film (annealed at 550 °C) is confirmed to be in the anatase phase in both the EBE and SG derived samples. The optical properties of the as-deposited n-TiO_2 TFs grown on p-SiNWs were analyzed using the Reflectance, Raman, and PL measurements. The as-fabricated p-SiNWs/n-TiO_2 based heterojunction

UV photodiode have excellent values of Detectivity, External Quantum Efficiency *(EQE)* or Gain, Responsivity and Contrast ratio with their respective values of ~8.66×10^{11} $mHz^{1/2}W^{-1}$, ~79.33 %, ~0.234 A/W and ~113.82 at -11 V in case of the EBE based samples and ~2.055×10^{11} $mHz^{1/2}W^{-1}$, ~21.543, ~0.65 A/W and ~1212.63 at -11 V for the SG based samples. The diode parameters such as rectification ratio, ideality factor and effective barrier height are ~519.82, ~5.49 and ~0.79 eV for EBE sample and ~673.25, ~6.62 and ~0.8379 eV for the SG based samples. The transient response characteristics of both types of heterojunction photodiodes under study have also been carried out. The electrical and optical properties of both the diodes appear to be very much promising for the nanoelectronic and optoelectronic applications.